We thank the Reviewer for the comments and suggestions to improve our paper. We feel the changes and additions we have made have improved the paper and provide a much better manuscript for the HESS audience. We have addressed each comment individually, below:

ANONYMOUS REFEREE #1

RECEIVED AND PUBLISHED: 14 JULY 2014

Summary: The paper investigates the utility of remote sensing products in the Noah- UCM framework in the LA basin, a highly urbanized area. The authors found that the remotely-sensed green vegetation fraction significantly enhances the Noah-UCM capability to reproduce evapotranspiration in urban areas. The authors also found that green vegetation fraction and impervious surface area improve the model capability to reproduce surface urban heat island effect (the difference in the land surface temperature between vegetated pixels and highly urbanized pixels). In my opinion, the paper is a significant contribution to the urban modeling field and shows that the modeling community should pay more attention to utilizing high-resolution remote sensing information in land surface models, especially urban models that require a lot of inputs. As such, I recommend acceptance for publication after minor revisions.

MAJOR COMMENTS:

1, My major concern is related to the forcing for the simulations. The authors used ten CIMIS and eight NCDC stations to generate the forcing for the simulations that cover an area of 49km2 at a spatial resolution of 30m. CMIS is used for solar radiation; NCDC is used for other variables; both are used for precipitation. Judging from Fig.1 one find that only 1 NCDC station is located in the study domain. All other stations are fairly far away from the study domain and some of them are strongly affected by other urban areas. This might cause some biases in the forcing that is supposed to represent the urban atmospheric conditions in the study domain. The authors may want to address this question since it might be the case that the biases in the atmospheric forcing are counteracted by some other biases that the remotesensing data sets introduce (just like the situation where the authors found including all remote-sensed parameters in the simulates reduces the performance of the model in reproducing ET as compared to only including GVF and ISA). The authors may also want to provide a figure showing the spatial distribution of some forcing variables such as radiation and temperature.

We appreciate the reviewer's comment. We want to point out that data scarcity is very common in urban areas and in the current work the authors tried to take advantage of any ground-based data that they had access to. Also, most of the forcing data come from NCDC stations. There is one NCDC station inside the study domain which is dominant in defining the forcing fields for this domain as the authors used 2nd power inverse-distance weighting to account for the spatial variability at the edges of our domain. Spatial maps of air temperature (Fig. 1r.a) and shortwave radiation (Fig. 1r.b) are presented below. We advocate that the forcing fields account for the influence of remote NCDC stations in the air

temperature case (Fig. 1r.a) and fairly homogeneous observations for different CIMIS stations in the shortwave radiation case (Fig. 1r.b).

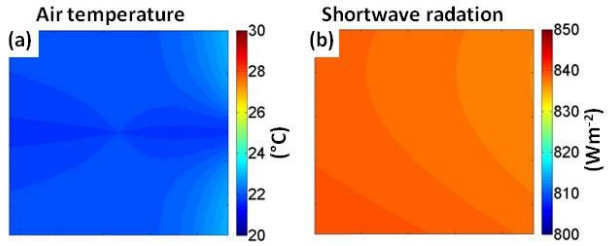

Figure 1r. Spatial maps of air temperature (a) and shortwave radiation (b), valid at 1100 LST on 14 April 2011.

2, It might be interesting to design a scenario in which irrigation is turned off and compare the sensitivity of the model to remote sensing information and the sensitivity to irrigation. The reason I raised this question is because in the validation of ET, the authors used the ET derived from CIMIS observations (using ETo and a landscape coefficient). Given that the simulations are also forced by CIMIS observations, there is some expectation that the Noah-UCM simulated ET should be consistent with the derived ET, as long as one considers the effect of landscape coefficient that is largely about irrigation. So I'm curious how much does irrigation contribute to the correlation between simulated and derived ET in Fig. 4a.

We thank the reviewer for this comment. First, we want to refer the reviewer to a recent paper from current authors (Vahmani and Hogue, 2014) where sensitivity of the Noah-UCM to incorporation of irrigation and different irrigation timings and intensities was investigated.

Also, the only CIMIS-based variable used to force the model was shortwave radiation. All other variables influencing simulated ET, including air temperature, longwave radiation, humidity, vegetation fraction, vegetation type, soil moisture/temperature, wind speed, and etc are independent from CIMIS station measurements. The fact that the CIMIS-based ET observations could be considered independent is proved in Fig. 4a where simulated and observed ET values illustrate very distinct behaviors when the default parameters are used.

References:

Vahmani, P. and Hogue, T. S.: Incorporating an Urban Irrigation Module into the Noah Land Surface Model Coupled with an Urban Canopy Model, J. Hydrometeorol., doi:10.1175/JHMD-13-0121.1, in press, 2014.

3, LST validation: first, can the authors comment on why there is no consistence in terms of R2 and RMSE across the last three scenarios in Fig. 6? Second, the authors attributed the underestimation of

LST values over high density residential and industrial/commercial areas to the surface temperature/ground heat flux scheme in the UCMs (lines 526 to 532), which I don't fully agree. If the authors used default LST value from UCM, which represents an aggregated surface temperature of the roof and the canyon, it is not a direct aggregation of the surface temperature of each component (roof+canyon). Instead, it uses the aggregated sensible heat flux (roof + canyon) and a turbulent transfer coefficient to infer an aggregated surface temperature that will produce the same amount of sensible heat flux. So the surface temperature calculations for each component should not significantly affect the aggregated surface temperature. Recently some inconsistence is found in the calculation of the turbulent transfer coefficient, at least in the WRF version of the Noah-UCM (Li, D., E. Bou-Zeid, 2014: Quality and Sensitivity of High-Resolution Numerical Simulation of Urban Heat Islands. Environmental Research Letters, 9, 055001 doi:10.1088/1748-9326/9/5/055001). The calculation of the turbulent transfer coefficient is using the roughness length of the non-impervious part of the same grid cell. This will cause some significant biases in the aggregated surface temperature.

We thank the reviewer for this very helpful comment. We re-ran our simulations, adopting the revised calculation of LST proposed by Li and Bou-Zeid [2014]. Using the new approach, the LST values over highly developed surfaces are significantly increased. This solves the LST underestimation problem in these areas (see revised Figs. 5 and 6). To implement the revised LST calculation, the following changes were made to the manuscript:

The following section is **ADDED** to the manuscript:

"*4.3. Improving the UCM-simulated LST*

The calculation of the impervious surface temperature in the UCM version used in this study has been shown to be inaccurate [Li and Bou-Zeid, 2014]. This is due to the fact that the turbulent transfer coefficient (C_h) for the whole pixel is calculated using only momentum and thermal roughness lengths of vegetated portion, ignoring the developed surface impact on C_h. Li and Bou-Zeid [2014] showed that this inconsistency could result in large biases in simulated LST values. In the current study, an alternative LST calculation, proposed by Li and Bou-Zeid [2014], is used as follows. First, a revised surface temperature of the impervious part of the pixel (T_s) is calculated based on canyon temperature (T_c) and roof surface temperature (T_r):

$$T_s = f_r \times T_r + (1 - f_r) \times T_c \qquad \text{Eq. (12)}$$

where f_r is the roof fraction of the impervious surface. Note that the T_c calculated by the UCM is an equivalent aerodynamic surface temperature aggregated for canyon surfaces, including walls and roads. Next, the LST for the whole grid cell is computed as a weighted average based on the T_s and surface temperature of pervious part (T_1):

$$LST = f_{urb} \times T_s + (1 - f_{urb}) \times T_1 \qquad \text{Eq. (13)}$$

where f_{urb} is the urban fraction of the pixel."

The following text was **REMOVED** from the manuscript (abstract):

"*However, the model still underestimates remotely sensed LST values over highly developed areas. We hypothesize that the LST underestimation is due to structural formulation in the UCM and cannot be immediately solved with available parameter choices."*

The followings are **REMOVED** from the manuscript (section 7.2):

"Further analysis (not shown here) indicates that underestimation of LST values is due to a fundamental problem in the UCM and cannot be immediately solved with available parameter choices. This problem is discussed in a related study investigating different schemes for LST and conductive heat fluxes in the UCM [Wang et al. 2011b]. Their study shows that the current UCM formulation results in a phase lag and cold biases in simulated surface temperature when compared to observations. The discussed cold biased could potentially be resolved utilizing a spatially-analytical scheme introduced by Wang et al. [2011b]."

"*Regardless of the parameterization processes, cold biases are persistent in all simulations, particularly over high intensity residential and industrial/commercial pixels (Fig. 6). As explained above, this underestimation of LST values is consistent with the literature and is reported to be due to a fundamental problem in the UCM which produces a phase lag and cold biases in simulated LST [Wang et al., 2011b].*"

The following is **REMOVED** from the manuscript (section 8):

"*Nevertheless, the model still underestimates remotely sensed LST values, over highly developed areas. We speculate that the underestimation of LST values, particularly over high intensity residential and industrial/commercial areas, is due to structural parameterization in the UCM and cannot be immediately solved with available parameter choices."*

The following figure is **REMOVED** from the manuscript:

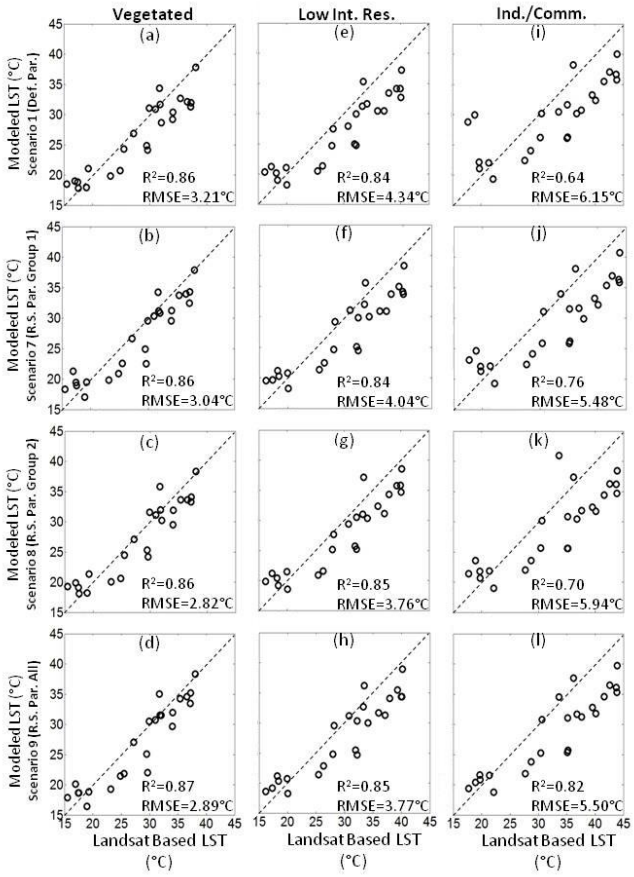

Figure 5. Scatter plots of observed (Landsat-based) versus simulated LSTs averaged over different land cover types using different urban surface parameterizations, including scenarios 1 (first row), 7 (second row), 8 (third row), and 9 (forth row) in Table 1.

The following figure is **ADDED** to the manuscript:

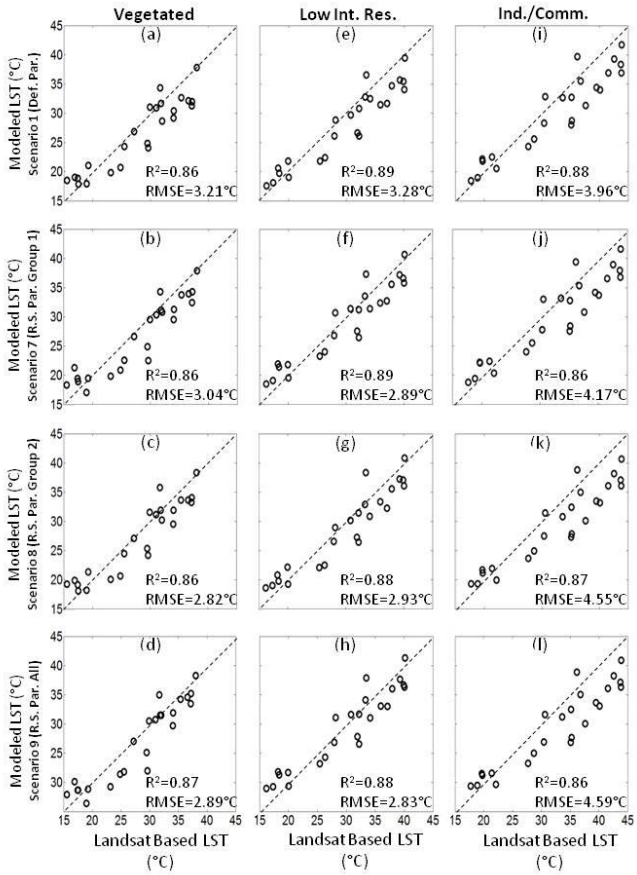

Figure 5. Scatter plots of observed (Landsat-based) versus simulated LSTs averaged over different land cover types using different urban surface parameterizations, including scenarios 1 (first row), 7 (second row), 8 (third row), and 9 (forth row) in Table 1.

The following figure is **REMOVED** from the manuscript:

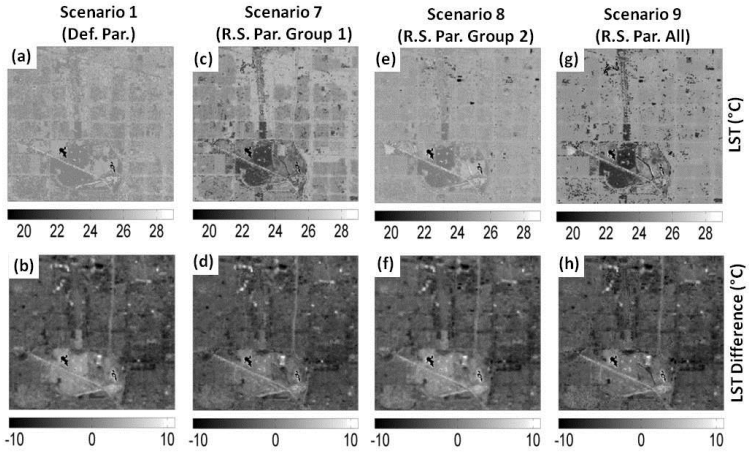

Figure 6. Noah/UCM simulated LST maps using different urban surface parameterizations: scenarios 1, 7, 8, and 9 from Table 1 (top row) as well as differences between simulated and observed land surface temperature at 1100 LST on 14 April 2011 (bottom row).

The following figure is **ADDED** to the manuscript:

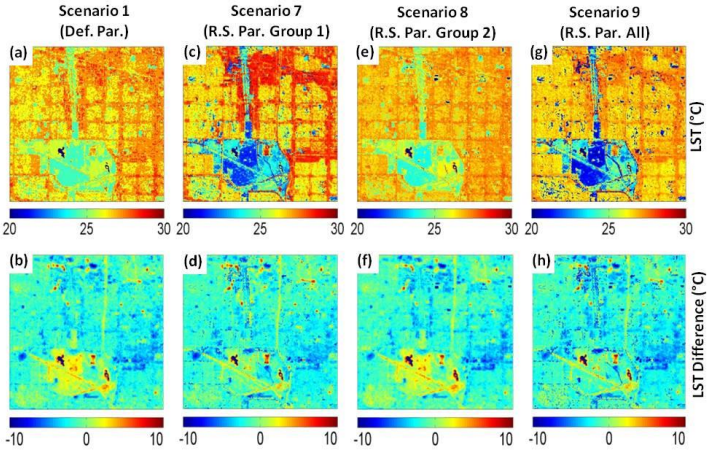

Figure 6. Noah/UCM simulated LST maps using different urban surface parameterizations: scenarios 1, 7, 8, and 9 from Table 1 (top row) as well as differences between simulated and observed land surface temperature at 1100 LST on 14 April 2011 (bottom row).

References:

Li, D., E. Bou-Zeid, 2014: Quality and Sensitivity of High-Resolution Numerical Simulation of Urban Heat Islands. Environmental Research Letters, 9, 055001 doi:10.1088/1748-9326/9/5/055001

High Resolution Land Surface Modeling Utilizing Remote Sensing Parameters and the Noah-UCM: A Case Study in the Los Angeles Basin

P. Vahmani[1] and T.S. Hogue[2,1]

[1]University of California, Los Angeles, CA

[2]Colorado School of Mines, Golden, CO

Re-submission to HESS

October 2014

Deleted: *Submitted*

Deleted: *April*

Corresponding Author:
Terri S. Hogue
Civil and Environmental Engineering
Colorado School of Mines
1500 Illinois Street
Golden, CO 80401
thogue@mines.edu
303-384-2588

ABSTRACT

In the current work we investigate the utility of remote sensing based surface parameters in the Noah-UCM (urban canopy model) over a highly developed urban area. Landsat and fused Landsat-MODIS data are utilized to generate high resolution (30 m) monthly spatial maps of green vegetation fraction (GVF), impervious surface area (ISA), albedo, leaf area index (LAI), and emissivity in the Los Angeles metropolitan area. The gridded remotely sensed parameter datasets are directly substituted for the land-use/lookup-table-based values in the Noah-UCM modeling framework. Model performance in reproducing ET (evapotranspiration) and LST (land surface temperature) fields is evaluated utilizing Landsat-based LST and ET estimates from CIMIS (California Irrigation Management Information System) stations as well as in-situ measurements. Our assessment shows that the large deviations between the spatial distributions and seasonal fluctuations of the default and measured parameter sets lead to significant errors in the model predictions of monthly ET fields (RMSE= 22.06 mm/month). Results indicate that implemented satellite derived parameter maps, particularly GVF, enhance the Noah-UCM capability to reproduce observed ET patterns over vegetated areas in the urban domains (RMSE= 11.77 mm/month). GVF plays the most significant role in reproducing the observed ET fields, likely due to the interaction with other parameters in the model. Our analysis also shows that remotely sensed GVF and ISA improve the model capability to predict the LST differences between fully vegetated pixels and highly developed areas.

Key words: Noah LSM, UCM, remote sensing, urban hydrology, evapotranspiration, Los Angeles

Deleted: However, the model still underestimates remotely sensed LST values over highly developed areas. We hypothesize that the LST underestimation is due to structural formulation in the UCM and cannot be immediately solved with available parameter choices.

1. Introduction

Urbanization introduces significant changes to land surface characteristics that ultimately perturb land-atmosphere fluxes of sensible heat, latent heat, and momentum which, in turn, alter atmospheric properties as well as local weather and climate [Landsberg, 1981; Kalnay and Cai, 2003; Miao et al., 2009; Ridder et al., 2012]. Urban surfaces are covered with variety of materials with distinct thermal, radiative, and moisture properties influencing surface energy and water budgets [Arnfield, 2003]. Moreover, contrasting aerodynamic properties of buildings significantly change surface roughness [Cotton & Pielke, 1995]. The effects associated with modified urban landscapes extend to air quality [Taha et al., 1997], local temperatures [Bornstein, 1987; Van Wevenberg et al., 2008], local and regional atmospheric circulation [Pielke et al., 2002; Marshall et al., 2004; Niyogi et al., 2006], and regional precipitation patterns [Changnon and Huff, 1986; Changnon, 1992; Lowry, 1998].

Mesoscale meteorological models have been increasingly applied over urban areas to examine the urban-atmosphere exchange of heat, moisture, momentum or pollutants. Recently updated parameterization in the community Weather Research and Forecasting (WRF) model includes coupling between the Noah LSM (Land Surface Model) and a single layer urban canopy model (UCM) [Kusaka et al. 2001; Kusaka and Kimura, 2004] which has substantially advanced the understanding and modeling of the mesoscale impact of cities. The coupled WRF-Noah-UCM has been applied to major metropolitan regions around the world (e.g. Houston, Beijing, Guangzhou/Hong Kong, , Salt Lake City, and Athens) to better understand the contribution of urbanization to changes in urban heat island, surface ozone, horizontal convective rolls, boundary layer structure, contaminant transport and dispersion, and heat wave events [Chen et al., 2004; Jiang et al., 2008; Miao and Chen, 2008; Miao et al., 2009; Wang et al., 2009; Tewari et al., 2010; Wei-guang et al., 2011; Giannaros et al., 2013]. A common concern with the use of these complex mesoscale models, however, is the high level of uncertainty in the specification of surface cover and geometric parameters [Loridan et al., 2010; Chen et al., 2011]. Although realistic

representation of surface properties is critical for accurate simulation of the physical processes occurring in urban regions, the majority of previous modeling studies rely on traditional land-use data and lookup tables to define surface parameters.

Remote sensed observations provide important spatial information on urban-induced physical modifications to the Earth's surface [Jin and Shepherd, 2005]. Airborne LIDAR (Light Detection and Ranging) systems and photogrammetric techniques have been utilized to produce morphological parameters over urban areas [Burian et al., 2004, 2006, 2007; Taha, 2008; Ching et al., 2009]. Burian et al. [2004] used airborne LIDAR data, at 1 m resolution, to generate datasets of 20 urban canopy parameters (e.g., building height, height-to-width ratio, and roughness length) for an air quality modeling study over Houston, Texas. Taha [2008] introduced an alternative and low-cost approach for generating urban canopy parameters input for the uMM5 over Sacramento region, California. The study relied on commercially available Google Earth PRO imagery to generate urban geometry parameters (e.g., pavement land-cover fraction, roof cover fraction, and mean building height). Using LIDAR-based three-dimensional data sets of buildings and vegetation, Ching et al. [2009] presented a high-resolution database of the geometry, density, material, and roughness properties of the morphological features for applications in WRF and other models over Houston, Texas. While promising, the availability of such datasets is currently limited to a few geographical locations and the reproduction of such datasets is extremely challenging due to high collection costs and data management difficulties associated with the extremely large size of LIDAR datasets [Burian et al., 2006; Ching et al., 2009].

Observations from satellites, on the other hand, have been utilized in model validation processes over urban areas [Miao et al., 2009; Giannaros et al, 2013]. In addition to in situ observations, Giannaros et al. [2013] included MODIS (Moderate Resolution Imaging Spectroradiometer) based Land Surface Temperature (LST) products in their modeling study of the urban heat island (UHI) over Athens, Greece. Similarly, Miao et al. [2009] utilized 1-km-resolution MODIS data to verify the WRF-Noah-UCM

Deleted: Tahah

simulated LST distribution in Beijing. Other studies have employed satellite data to replace outdated urban land use maps in atmospheric models with new remote sensing products [Cheng and Byun, 2008; Cheng et al., 2013]. Focusing on boundary layer mixing conditions and local wind patterns in the Houston Ship channel, Cheng and Byun [2008] reported that the Noah LSM and planetary boundary layer (PBL) scheme performances in the MM5 were improved when land-use type distributions were correctly represented in the model using high resolution Landsat-based land use data. Cheng et al. [2013] compared WRF simulations in the Taiwan area using U.S. Geological Survey (USGS), MODIS, and SPOT (Système Pour l'Observation de la Terre) based land use data. Using the new high resolution land use types obtained from SPOT satellite imagery, the WRF predictions of daytime temperatures and onshore sea breezes had the best agreement with observed data. Furthermore, more accurate surface wind speeds were simulated when MODIS and SPOT data replaced conventional USGS land use maps in the WRF runs due to the more realistic representation of roughness length in the remotely sensed databases. Although these and other previous studies [e.g., Jin and Shepherd, 2005] have recognized the usefulness of satellite imagery (e.g., NASA's Terra, Aqua, and Landsat data) in specifying surface physical characteristics in urban environments, very few have directly incorporated high resolution gridded satellite-based parameters (e.g., impervious surface area, albedo, and emissivity) into parameter estimation within land surface/atmospheric modeling systems.

In the current work we investigate the utility of remote sensing based surface parameters in the Noah-UCM modeling framework over a highly developed urban area. Among parameters that can be related to a measurable physical quantity, we evaluate those routinely and freely obtained from satellite-based platforms. The derived parameter sets are implemented in the Noah-UCM with a focus on simulated surface energy and water cycles that are essential feedback to the widely used WRF model. Landsat and fused Landsat-MODIS data are utilized to generate high resolution (30 m) monthly spatial maps of green vegetation fraction (GVF), impervious surface area (ISA), albedo, leaf area index

Deleted: later

(LAI), and emissivity in the Los Angeles metropolitan area. The temporal and spatial distributions of newly assigned parameters are compared with those based on the model lookup tables. Next, gridded remotely sensed parameter datasets are directly incorporated into the Noah-UCM modeling framework replacing the land-use/lookup-table-based values. The sensitivity of the simulated energy and water fluxes to the newly developed spatial metrics of parameters is presented. The model's performance in reproducing evapotranspiration (ET) and LST fields is evaluated utilizing Landsat-based land surface temperature and ET estimates from CIMIS (California Irrigation Management Information System) stations as well as in-situ measurements. Finally, the influence of each parameter set on the urban energy and water budgets is investigated.

2. Study Area

The study domain is a 49 km^2 highly developed neighborhood in the City of Los Angeles (Fig. 1). Los Angeles is the second most populous city in the United States with a population of 3.8 million [U.S. Census, 2011], covering an area of 1,215 km^2 in Southern California. The City has a Mediterranean climate and receives 381 mm of annual precipitation, mostly over the winter months [NOAA-CSC, 2003; SCDWR, 2009]. Due to the semi-arid nature of the region, the City's water supply is heavily dependent on imported water (52% from the Colorado River and 36% from the Los Angeles Aqueduct) [LADWP, 2010]. Regional water demands and the extensive dependence on external sources make accurate spatial representation of the metropolitan area in regional land surface/atmospheric models imperative for predicting current and future water budgets. The study domain includes commercial/industrial as well as low and high intensity residential land cover types and a large park with both irrigated and non-irrigated landscapes (Fig. 1b and 1c).

299 **3. Remotely Sensed Parameters**

300 Remote sensing data are retrieved from Landsat ETM+ images with a nominal pixel resolution of 30 m in
301 the short wave bands and 60 m in the thermal band. The level 1Gt ETM+ imagery from USGS EROS,
302 spanning years 2010-2011, are calibrated and atmospherically corrected through the Landsat Ecosystem
303 Disturbance Adaptive Processing System (LEDAPS). Study domain data are not affected by the failure of
304 the Landsat-7 ETM+ Scan Line Corrector in 2003 (SLC-off). Employing a knowledge-based approach,
305 similar to the one introduced by Song and Civco [2002], several binary masks are applied to the images
306 to detect contaminated areas (cloud and shadow). Images with cloud and/or shadow are distinguished
307 and omitted in the following parameter retrievals. A total of 24 pure images, acquired over two years,
308 are utilized in the parameter estimation processes.

309 In addition to Landsat observations, MODIS products from Terra and Aqua satellite platforms
310 are also utilized. The MODIS MCD43A BRDF (Bidirectional Reflectance Distribution Function) products,
311 concurrent with pure Landsat images, are collected for use in the parameter calculations. The 500-m
312 BRDF products are generated by the MODIS Adaptive Processing System (MODAPS) at the Goddard
313 Space Flight Center (GSFC), using a kernel-driven linear model, and distributed through the Land
314 Processes DAAC (Distributed Active Archive Center) [Justice et al., 2002; Schaaf et al., 2002; Shuai et al.,
315 2008]. The described Landsat and MODIS-based data are used to produce a group of six remotely sensed
316 derivatives:

317 • *Green Vegetation Fraction (GVF):* GVF spatial maps are derived according to Gutman and
318 Ignatov [1998] utilizing NDVI (Normalized Difference Vegetation Index) measurements. First,
319 atmospheric corrected reflectance values from the red (ρ_{ETM3}) and near-infrared (ρ_{ETM4}) bands of Landsat
320 ETM+ are used to derive NDVI maps for each date of imagery based on Eq. 1. Next, assuming the
321 vegetated part of a pixel is covered by dense vegetations (i.e., it has a high LAI), GVF is calculated using
322 Eq. 2.

Deleted: 2033

$$NDVI = \frac{\rho_{ETM4} - \rho_{ETM3}}{\rho_{ETM4} + \rho_{ETM3}} \quad \text{Eq. (1)}$$

$$GVF = \frac{NDVI - NDVI_o}{NDVI_\infty - NDVI_o} \quad \text{Eq. (2)}$$

Where $NDVI_o$ and $NDVI_\infty$ are constant values computed using signals from bare soil and densely vegetated pixels in the study domain, respectively.

- *Impervious Surface Area (ISA):* ISA is shown to be inversely proportional to vegetation fraction where non-vegetated pervious surfaces are rare [Bauer et al., 2007]. Since the majority of pervious surfaces in the studied domain are vegetated and heavily irrigated throughout the year, ISA is assumed to be the complement of the vegetation fraction:

$$ISA = (1 - GVF_{max}).100 \quad \text{Eq. (3)}$$

Where GVF_{max} is the maximum GVF detected over the two year study period. The produced ISA map shows high accuracy (>95%) when compared to a previously developed high resolution land cover map, based on QuickBird remote sensing data, aerial photographs, and geographic information systems over the city of Los Angeles [McPherson et al., 2008]. We speculate that one cause contributing to the high accuracy of this assumption is that ISA overestimation, induced by non-vegetated pervious surfaces, is offset by tree canopies that cover areas larger than underlying pervious surfaces.

Deleted: that may contribute

- *Albedo:* Employing a recent methodology by Shuai et al. [2011], 30 m land surface albedo maps is generated utilizing Landsat surface reflectance and anisotropy information from concurrent 500 m MODIS BRDF products. Landsat data are reprojected from UTM to MODIS sinusoidal projection and aggregated from 30 m to 500 m. Using USGS-based land cover types, the percentage of each land cover class within each MODIS pixel is computed, then relatively pure pixels (>85% purity) are selected for each class. MCD43A2 quality assessment product is used to choose highest quality MODIS MCD43A1

BRDF parameters for the pure pixels. The concurrent parameters are used to calculate nadir reflectance, white sky albedo, and black sky albedo under the solar geometry at Landsat overpass time and MODIS scale. Next, the spectral albedo-to-nadir reflectance ratios, for white sky and black sky albedos, are calculated over the pure pixels. The resultant ratios, specific to each land cover class, are applied to Landsat surface reflectance to generate the spectral white sky and black sky albedos for each Landsat pixel. A further narrowband-to-broadband conversion based on extensive radiative transfer simulations by Liang [2000] is applied to generate the broadband albedos at shortwave regime. Finally, albedo (blue sky) is modeled as an interpolation between the black sky (α_{bs}) and white sky (α_{ws}) albedos as a function of the fraction of diffuse skylight ($S(\theta,\tau(\lambda))$ which is estimated by the 6S (Second Simulation of the Satellite Signal in the Solar Spectrum) codebase (Eq. 4) [Schaaf et al., 2002].

$$\propto(\theta,\lambda) = \{1 - S(\theta,\tau(\lambda))\}\alpha_{bs}(\theta,\lambda) + S(\theta,\tau(\lambda))\alpha_{ws}(\theta,\lambda) \qquad \text{Eq. (4)}$$

where τ, θ, and λ are optical depth, solar zenith, and wavelength, respectively.

- *Leaf Area Index (LAI):* Stenberg et al. [2004] showed that a reduced simple ratio (RSR) explains 63%-75% of the variations in LAI and that maps of projected LAI, based on RSR, have good agreement with observations. In the current study, LAI values are retrieved based on the LAI-RSR correlations which are specified utilizing table-based LAI estimates in pure (fully vegetated) pixels and remotely sensed RSR maps. The atmospheric corrected reflectance values of Landsat ETM spectral channels red (ρ_{ETM3}), near infrared (ρ_{ETM4}), and mid infrared (ρ_{ETM5}), implemented in the following equation (Eq. 5), define RSR:

$$RSR = \frac{\rho_{ETM4}}{\rho_{ETM3}} \cdot \frac{\rho_{5_{max}} - \rho_{ETM5}}{\rho_{5_{max}} + \rho_{5_{min}}} \qquad \text{Eq. (5)}$$

where $\rho_{ETM5min}$ and $\rho_{ETM5max}$ are the smallest and largest mid infrared reflectance detected in the Landsat ETM images over the study domain, excluding open water pixels.

- *Emissivity:* Among various methods developed to define land surface emissivity, the NDVI Thresholds Method ($NDVI^{THM}$) has been widely applied to urban areas [Stathopoulou and Cartalis, 2007; Stathopoulou et al., 2007; Tan and Li, 2013]. $NDVI^{THM}$ is superior to other methods since the consideration of the internal reflections (cavity effects), caused by heterogeneous surfaces minimizes the overall error in this approach [Sobrino et al., 2001]. This methodology, originally introduced by Sobrino and Raissouni [2000] and modified later by Stathopoulou et al. [2007] for urban areas, is selected for land surface emissivity estimation in the current work. Using the Landsat-based NDVI thresholds, the study area is divided into four classes: (1) fully vegetated (NDVI>0.5), (2) built-up areas with sparse vegetation (NDVI≤0.2), (3) mixture of man-made material and vegetation (NDVI>0.2 and ≤0.5), and (4) water bodies (NDVI<0). Mean emissivity values of 0.980, 0.920, and 0.995 are then used for fully vegetated, built-up and water pixels [Similar to Tan and Li, 2013]. Emissivity values (ε) for mixed pixels (class 3) are estimated using the following equations [for details see Stathopoulou et al., 2007]:

$$\varepsilon = 0.017P_V + 0.963 \qquad \text{Eq. (6)}$$

$$P_V = \frac{(NDVI-0.2)^2}{(0.5-0.2)^2} \qquad \text{Eq. (7)}$$

- *Land Surface Temperature (LST):* The emissivity corrected land surface temperature (LST) is calculated as follows [Artis & Carnahan, 1982]:

$$LST = \frac{BT}{\left\{1+\left[\frac{\lambda . BT}{\rho}.\ln \varepsilon\right]\right\}} \qquad \text{Eq. (8)}$$

where BT is Landsat at sensor brightness temperature (K); λ and ε are the wavelength of emitted radiance (11.5 µm) and surface emissivity; $\rho = hc/\sigma$ ($1.438 \times 10^{-2} m\ K$); σ, h, and c are Boltzmann constant, Planck's constant, and the velocity of light, respectively.

4. Numerical Modeling System

4.1. Noah LSM-UCM Model

Land surface processes are parameterized using the offline Noah LSM [Chen and Dudhia, 2001] coupled with the single layer UCM [Kusaka et al. 2001; Kusaka and Kimura, 2004]. The Noah LSM is based on a diurnally dependant Penman potential evaporation approach, a multi-layer soil parameterization, a canopy resistance model, surface hydrology, and frozen ground physics [Chen et al., 1996, 1997; Chen and Dudhia, 2001; Ek et al., 2003]. The UCM parameterization includes urban building geometry, shadowing from buildings, reflections and trapping of radiation in a street canyon, and an exponential wind profile. The Noah LSM provides surface sensible and latent heat fluxes and surface skin temperature for vegetated areas (e.g., parks and trees) and the UCM calculates the fluxes for impervious surfaces. The outputs from the Noah LSM and UCM are coupled through the urban surface fractions.

4.2. Irrigation Module

Irrigation is accounted for, in the Noah-UCM modeling framework, by incorporating an urban irrigation module developed in our previous work [Vahmani and Hogue, 2013; 2014]. The developed irrigation scheme mimics the effects of urban irrigation by increasing soil moisture content in vegetated portion of grid pixels at a selected interval. Added anthropogenic soil moisture contribution is a function of the soil moisture deficit, which is the difference between irrigated soil moisture content and actual soil moisture content in the top soil layer. The irrigation module calculates irrigated soil moisture content (SMC_{IRR}; m^3 m^{-3}), soil moisture deficit (DEF; m^3 m^{-3}), and irrigation water (IRR; kg m^{-2} s^{-1}) as:

$$SMC_{IRR} = \alpha . SMC_{max} \quad \text{Eq. (9)}$$

$$DEF = \max\{[SMC_{IRR} - SMC_1], 0\} \quad \text{Eq. (10)}$$

$$IRR = \frac{\rho_w}{\Delta t} DEF . D_1 \quad \text{Eq. (11)}$$

where saturation soil moisture content (SMC_{max}; $m^3\ m^{-3}$) and irrigation demand factor (α; unit less) define irrigated soil moisture content (Eq. 9); D_1 is top soil layer thickness (10 cm); ρ_w ($kg\ m^{-3}$)and Δt stand for water density and Noah-UCM time step (3600 s), respectively. The parameter α, ranging from zero to one, regulates the amount of irrigation water added to the soil each time the scheme increases the soil moisture, simulating an irrigation event. Similar to previous studies [Hanasaki et al. 2008a, 2008b; Pokhrel et al. 2012] an irrigation demand factor of 0.75 is utilized in the current work. The irrigation interval is set to three times per week according to the water restrictions implemented by Los Angeles Department of Water and Power (LADWP) in 2010 (LADWP, personal communication, 2013).

4.3. Improving the UCM-simulated LST

Deleted: 4.3.

The calculation of the impervious surface temperature in the UCM version used in this study has been shown to be inaccurate [Li and Bou-Zeid, 2014]. This is due to the fact that the turbulent transfer coefficient (C_h) for the whole pixel is calculated using only momentum and thermal roughness lengths of vegetated portion, ignoring the developed surface impact on C_h. Li and Bou-Zeid [2014] showed that this inconsistency could result in large biases in simulated LST values. In the current study, an alternative LST calculation, proposed by Li and Bou-Zeid [2014], is used as follows. First, a revised surface temperature of the impervious part of the pixel (T_s) is calculated based on canyon temperature (T_c) and roof surface temperature (T_r):

$$T_s = f_r \times T_r + (1 - f_r) \times T_c \quad \text{Eq. (12)}$$

where f_r is the roof fraction of the impervious surface. Note that the T_c calculated by the UCM is an equivalent aerodynamic surface temperature aggregated for canyon surfaces, including walls and roads. Next, the LST for the whole grid cell is computed as a weighted average based on the T_s and surface temperature of pervious part (T_1):

$$LST = f_{urb} \times T_s + (1 - f_{urb}) \times T_1 \quad \text{Eq. (13)}$$

where f_{urb} is the urban fraction of the pixel.

4.4. Land Cover Data and Forcing Fields

The Noah-UCM modeling system requires static data to describe physical characteristics of the surface, including soil type, slope type, vegetation type, and urban type. A combination of the Soil Data Mart [http://soildatamart.nrcs.usda.gov] and the Los Angeles Department of Public Works (LADPW) databases are used to gather soil classification information. Land use and land cover are parameterized using the 30 m NOAA C-CAP-2006 land cover data which is transformed to urban and vegetation type spatial maps over the study domain. High, medium, and low intensity developed land cover types, recognized by NOAA, are converted to UCM Industrial/Commercial, high and low intensity residential types, respectively. The developed open space along with natural land types are categorized as one of the 27 Noah LSM vegetation classes.

The offline Noah LSM-UCM is forced utilizing hourly ground-based observations from CIMIS and National Climatic Data Center (NCDC) stations for the period from 1 January 2010 to 31 December 2011. There are ten CIMIS and eight NCDC stations within close proximity of the study domain (Figure 1a). The NCDC stations, which use Automated Surface Observing Systems (ASOS), are located at smaller local airports (6 stations), one major airport (Los Angeles International Airport), and a university campus (University of Southern California; USC) within the Los Angeles metropolitan area. Reporting the meteorological conditions, the NCDC stations are used for wind speed, air temperature, relative humidity, air pressure, and incoming long wave radiation. All NCDC data are gathered at a standard reference height of 2m. The regional CIMIS stations are utilized for solar radiation (using LI200S pyranometer) and tipping bucket rain gauges in 18 stations (NCDC and CIMIS) are included in collection of precipitation data. Inverse-distance weighting (2^{nd} power) is employed to create the spatial gridded forcing fields. Linear interpolation and data from the nearest gage are utilized to replace missing data.

5. Numerical Experiments and Evaluation Methods

5.1. Remote Sensing Based Parameterization

To investigate the sensitivity of the Noah-UCM model to integration of the developed remotely sensed parameters, nine simulation scenarios are designed (Table 1). A control experiment (Scenario 1) is conducted in which all default parameters are utilized in the Noah-UCM. Scenarios 2 to 6 explicitly assess each individual parameter effects on urban energy and water budgets using the newly incorporated remote sensing parameters. Scenario 7 analyzes the effects of employing both remotely sensed GVF and ISA while Scenario 8 assesses simultaneous integration of albedo, LAI, and emissivity. We are interested in the comparison of Scenarios 7 and 8 as the Noah-UCM parameterizations use GVF and ISA to select albedo, LAI, emissivity, and roughness length values from the predefined ranges in the parameter tables. It is worth mentioning that GVF alters the roughness length values over pervious or natural areas. However, roughness length and building height over the impervious surfaces are kept at the default values listed by Chen et al. [2011]. Scenarios 7 and 8 help quantify the contribution of each parameter group to the model's ability to reproduce the observed surface states and fluxes. Finally, the last experiment (Scenario 9) implements all five remotely sensed parameter sets in the simulations. It should be noted that the GVF and LAI measurements over mixed pixels (vegetated urban areas) are scaled up by multiplying the remotely sensed values by 1/(1-urban fraction) since in the Noah-UCM modeling framework these parameters characterize only the pervious portion (1 - urban fraction) of each pixel. However, remotely sensed albedo and emissivity values over each pixel are assigned to both pervious and impervious surfaces for that pixel. Other than the implemented remote sensing based parameters, the rest of the model parameters are kept at default values. All experiments incorporate the irrigation module and irrigation rates are kept constant in all scenarios. All scenarios are run at 30 m spatial and 1 hour temporal resolutions, spanning 2010 and 2011, with the first three months used as model initialization.

Deleted: using urban fractions

Deleted: ,

Deleted: ,

Deleted: sending

5.2. Model Evaluation Approach

In order to evaluate the performance of the Noah-UCM modeling framework, simulated LSTs are compared with concurrent Landsat observations and simulated latent heat flux time series are assessed against CIMIS-based ET observations. The CIMIS network was established in 1982 by the CDWR (California Department of Water Resources) and the University of California at Davis in order to provide real-time weather conditions and irrigation water need estimates for California's agricultural community. The automated CIMIS stations measure hourly surface solar radiation, temperature, humidity, wind, precipitation, soil temperature, and surface pressure [http://wwwcimis.water.ca.gov]. Employing observed meteorological fields over a well-watered soil, the reference ET (ET_0) is calculated for each site. Utilizing a methodology introduced by CDWR [2000], actual urban landscape ET is estimated using ET_0 and a landscape coefficient, which is a function of species, density, and microclimate factors. Based on the authors' knowledge in the study landscape as well as a report by CDWR [2000], we assume "Moderate" (trees and shrubs) and "High" (turf grass) water needs. Following the CDWR [2002] instructions on irrigation zones with mixed water need categories (i.e., low, moderate, and high), a value from high category is selected (average species factor=0.80). Assuming the "average" category for vegetation density, a density factor of 1 is used. Furthermore, a "high" category of microclimate condition is used (microclimate factor=1.25) for the current highly developed study domain. This factor is utilized to take into account the contribution of the developed surfaces to the water loss from vegetated areas, through anthropogenic heating, reflected light, and high temperatures of surrounding heat-absorbing surfaces (e.g., paving and buildings). Using these factors, a landscape coefficient of 1 (landscape coefficient = species factor × density factor × microclimate factor) is prescribed. This coefficient and ET_0 estimations from ten CIMIS stations within close proximity of the study domain (Fig. 1a) are utilized to compute the urban landscape ET. Inverse-distance weighting (2nd power) is employed to create spatial gridded ET maps over fully vegetated pixels in the study area which is then used in validation processes of the Noah-UCM. ET output of the model is also evaluated against

Deleted: /cimis

513 recent ET measurements in the greater Los Angeles area [Moering, 2011]. Moering [2011] employed a
514 previously developed chamber approach to measure instantaneous ET in an irrigated and a non-
515 irrigated park in the Los Angeles metropolitan area during WY (Water Year) 2011 (WY is defined as Oct.
516 1st of the previous year to Sep. 30th of the designated year). They reported an annual ET of about 1224
517 mm over the observed irrigated park, which is located within our study domain.
518
519 **6. Sensitivity Study of Surface Parameters**
520 **6.1. Temporal Evaluation**
521 The monthly time series of the default Noah-UCM and remote sensing based GVF, ISA, albedo, and LAI
522 are compared and modeled cumulative monthly sensible and latent heat fluxes, using default and newly
523 estimated parameters, are presented over fully vegetated, low intensity residential, and
524 industrial/commercial areas (Fig. 2). Fluxes from high intensity residential areas are not presented as
525 they behave similarly to those from the industrial/commercial areas. Except for the summer months,
526 GVF values are significantly increased throughout the year when remote sensing products are utilized
527 (Fig. 2a). Moreover, the default seasonal variations of GVF values, assumed over all the land cover types,
528 are not detected in Landsat imagery (Fig. 2a). The reason for this is the significant and year round
529 irrigation in the Los Angeles area, which is not accounted for in the default parameter tables. This is
530 confirmed by previous studies [Johnson and Belitz, 2012] that reported urban vegetation supported by
531 water delivery, in contrast to common seasonal behavior of greening in the winter/spring and browning
532 in the summer, maintains constant greenness which is reflected in NDVI and GVF estimates. GVF plays a
533 dominant role in the Noah-UCM simulations as it defines the vegetated fraction of the natural areas,
534 and specifies albedo, LAI, emissivity, and roughness length values from the predefined ranges in the
535 model lookup tables. Furthermore, GVF partitions the total ET between soil direct and canopy ET. The
536 simulated latent heat flux is considerably decreased (up to 139 MJ m^{-2} per month) in the summer time

and increased over the remaining months, when remotely sensed GVF is incorporated in the fully vegetated areas (Fig. 2b). Since any increase of latent heat flux that does not alter the radiative balance leads to a reduction in sensible flux, the newly developed GVF values, in turn, cause enhancements (up to 103 MJ m^{-2} per month) in the simulated summer sensible heat fluxes and a reduction in the sensible heat fluxes during the remaining months (Fig. 2b). Latent and sensible heat fluxes from the low intensity residential pixels show similar but less significant changes (up to 66.1 and 31.0 MJ m^{-2} per month, respectively), when the new parameter sets are implemented. Adding remotely sensed GVF causes insignificant changes in the industrial/commercial area fluxes due to the small percentage of vegetated land cover in such areas (Fig. 2d).

There are also large deviations between the look-up-table-based ISAs and the remotely sensed values. Averaged ISA is decreased (10%) over industrial and commercial pixels and increased (49%) over low intensity residential areas, when remote sensing products are utilized in the parameter estimation process (Fig. 2.e). These changes in the impervious surface area, or urban fraction values, have significant effects on monthly latent and sensible heat fluxes over the developed pixels (Fig. 2g and 2h), due to the critical role of urban fraction in partitioning of the energy fluxes. Over the low intensity residential areas, higher ISA values minimize the effects of urban vegetation which leads to latent heat fluxes decreases (up to 62.6 MJ m^{-2} per month) and sensible heat fluxes increases (up to 52.4 MJ m^{-2} per month), throughout the year, when remotely sensed data replace default urban fractions (Fig. 2g). These changes are reversed and less significant over the industrial and commercial pixels (maximum latent and sensible heat flux changes of 30.0 and 26.5 MJ m^{-2} per month, respectively; Fig. 2h). ISA has no influence on the fluxes from fully vegetated pixels which do not include impervious areas (Fig. 2.f).

Considerable changes in the monthly albedo averages are detected when incorporating remote sensing data in the parameterization process (Fig. 2i). Using fused Landsat and MODIS products, a reduction of averaged albedo values is observed over the fully vegetated and residential areas (up to

Deleted: MOSID

562 48% and 39%, respectively; Fig. 2i). Moreover, the default seasonal variations are hardly noticeable in
563 the remote sensing based albedo values, which is due to the consistent greenness in the study area from
564 irrigation throughout the year. On the other hand, considerable albedo increases (up to 39%) are
565 detectable over the industrial/commercial pixels (Fig. 2i), which are caused by bright and highly
566 reflective materials seen mainly over the rooftops of industrial/commercial buildings. Albedo affects the
567 radiative energy budget and consequently available energy for the turbulent fluxes. In the current study,
568 decreased albedo values over the fully vegetated and low intensity residential areas result in reduced
569 loss of solar and long wave radiation respectively and, in turn, increases the sensible heat flux (up to
570 33.8 and 21.5 MJ m^{-2} per month; Fig. 2j and 2k). Albedo induced sensible heat deceases over
571 industrial/commercial pixels are also noticeable (up to 33.9 MJ m^{-2} per month; Fig. 2l).
572 Distinct seasonal fluctuations of LAI are observed in the remotely sensed data and the default parameter
573 tables (Fig. 2m). This reflects the fact that landscape plantings are quite different from agricultural crops
574 due to their being composed of collections of vegetation species and affected by complex irrigation
575 patterns which are not taken into account in the vegetation parameter tables in the Noah LSM [CDWR,
576 2000; Vahmani and Hogue, 2013; 2014]. Over the heavily vegetated pixels, the default pattern is
577 reversed in the measured parameter sets with less seasonal variations and peaks in the winter time, due
578 to the fact that most of the precipitation occurs in the winter months, over the current study domain
579 (Fig. 2m). The industrial and commercial pixels illustrate higher LAI values in the remotely sensed
580 parameter maps, year round, when compared to the default values (Fig. 2m). LAI is a critical parameter
581 in the Noah LSM, which is involved in the parameterization of the canopy resistance, controlling canopy
582 ET rates. In the presented results (Figs. 2n and 2o), LAI induced changes in the simulated turbulent fluxes
583 are more apparent in the summer months and over fully vegetated and residential pixels, where
584 sensible heat flux is significantly increased (up to 57.2 and 86.5 MJ m^{-2} per month, respectively) and
585 latent heat flux is significantly decreased (up to 65.5 and 97.9 MJ m^{-2} per month, respectively). This is

586 due to the considerable deceases in the LAI values in summer time which lead to elevations of the
587 canopy resistance and therefore reductions of the transpiration from the vegetation, causing decreases
588 in latent heat fluxes. This in turn partitions the net radiation more into sensible heat fluxes. LAI does not
589 affect fluxes from industrial/commercial pixels with small pervious fractions (Fig. 2p). It is worth
590 mentioning that changes in the turbulent fluxes time series, in particular the latent heat flux decreases
591 in the summer months induced by implementation of satellite-based LAI, are to some extent captured in
592 the simulations with the remote sensing based GVF (compare Fig. 2b with 2n and 2c with 2o). This
593 reflects our previous point that GVF controls assigned LAI values to vegetated pixels in the Noah LSM
594 and that realistic presentation of GVF in the modeling framework can enhance LAI inputs in the model
595 when LAI measurements are not available.
596 Remotely sensed emissivity maps are also utilized to replace the default values in the Noah-
597 UCM simulations, which results in changes in the emissivity values (up to 5.1%). However, the new
598 surface parameterization leads to insignificant changes in turbulent fluxes (results now shown). The
599 largest emissivity induced alterations in sensible heat fluxes are seen over industrial and commercial
600 pixels (up to 31.2 MJ m^{-2} per month). Latent heat fluxes are changed, the most significantly, over fully
601 vegetated areas (up to 2.56 MJ m^{-2} per month).
602 **6.2. Spatial Evaluation**
603 The spatial distributions of newly assigned GVF, ISA, albedo, and LAI are next compared with those
604 based on the Noah-UCM lookup tables. Different urban surface parameterizations, along with their
605 impacts on the simulated maps of turbulent sensible and latent heat fluxes, are presented (Fig. 3; Valid
606 at 1100 LST on 14 April 2011). As expected, during the spring period (April), GVF values are significantly
607 higher when remote sensing products are utilized, due to the irrigation effects which are ignored in the
608 default parameters (Fig. 3a and 3b). Over fully vegetated and low intensity residential pixels, where a
609 significant portion of the energy goes into evaporation and transpiration, latent heat flux increases

(about 300 and 230 W m^{-2}, respectively) and sensible heat fluxes decreases (about 160 and 120 W m^{-2}, respectively) are found (Fig. 3c and 3d) when utilizing the remote sensing GVF.

The spatial distributions of ISA, or urban fraction, between the remote sensing and default values show similar patterns (Fig. 3e and 3f). However, industrial/commercial and high intensity residential areas are assigned noticeably higher urban fraction values in the remote sensing based maps (compare Fig. 3e and 3f) which leads to lower latent heat fluxes (bias of up to about 130 W m^{-2}) and higher sensible (bias of up to about 100 W m^{-2}) in these pixels (Fig. 3g and 3h).

The Noah-UCM parameters, based on look-up tables, underestimate surface albedo values over highly urbanized pixels, when compared with remote sensing data (Fig. 3i and 3j). In particular, the industrial/commercial buildings with highly reflective rooftops are completely ignored. Over the highly vegetated areas, however, albedo values are slightly overestimated in look-up tables. Altering the energy budget, the newly developed albedo datasets lead to lower Noah-UCM-simulated sensible heat fluxes over intensely developed pixels (Fig. 3k). The sensible heat flux differences are only significant over industrial/commercial pixels which include buildings with bright roofs (up to ~300 W m^{-2}). The changes in absolute surface albedos do not affect simulated latent heat fluxes as these reflective roofs are located in industrial/commercial areas with negligible pervious surfaces and simulated latent heat flux (Fig. 3l).

The remote sensing data detect higher LAI values over all pixel types, particularly over fully vegetated areas where new LAI values are significantly higher (Fig. 3m and 3n). By influencing the canopy resistance, these changes redefine the spatial distribution of turbulent fluxes (Fig. 3o and 3p). Over the densely vegetated areas, increases in latent heat flux (up to 50 W m^{-2}) and decreases in sensible heat flux (up to 35 W m^{-2}) are found (Fig. 3o and 3p). It is noteworthy that, as illustrated before (Fig. 3n and 3o), the most significant influences of LAI alterations are detected in the summer months.

Deleted: in the default parameterization.

Deleted: and higher fluxes over the vegetated areas

Deleted: the most

Deleted: ; Fig. 3k

Deleted: (Fig.

Thus, it is not surprising that the turbulent fluxes do not show significant sensitivity to the LAI changes in April.

Remotely sensed emissivity maps, implemented in the Noah-UCM simulations, show minimal effect on the output turbulent fluxes maps (results not shown). Our results (Fig. 2 and 3) agree with previous sensitivity studies performed with the Noah-UCM which indicated high sensitivity of the model to GVF, ISA, albedo, and LAI, and less model sensitivity to emissivity [Loridan et al., 2010; Wang et al., 2011]. Loridan et al. [2010] highlighted the critical role of ISA and LAI in the simulations of latent heat flux and albedo role in the sensible heat flux simulations. Investigating the peaks of diurnal turbulent fluxes, Wang et al. [2011] reported that latent heat flux is the most sensitive to the GVF. They also found that emissivity has minimal effects on the model outputs.

7. Evaluation of Noah-UCM Performance

After initial sensitivity tests, the model performance in reproducing ET and LST fields is evaluated using remotely sensed (independent from derived parameters) and in situ measurements. The comparisons of observed and simulated ET and LST, using different urban surface parameterizations (scenarios 1, 7, 8, and 9 in Table 1), are presented in figures 4, 5, and 6.

7.1. ET Simulations

The temporal variations of ET, simulated by the Noah-UCM model and averaged over fully vegetated pixels, are evaluated against CIMIS-based ET measurements, spanning 2010 and 2011 (Fig. 4). The presented observations are averages over fully vegetated pixels in the study domain, calculated using ET maps based on ET_0 measurements from ten CIMIS stations, landscape coefficients, and inverse-distance weighting (2^{nd} power) (see section 5.2). The model reproduces similar ET behaviors when the default parameters and the second group of remotely sensed parameters (albedo, LAI, and Emissivity) are implemented (Fig. 4a and 4c). The ET differences between observations and the default simulation are

Deleted: 4).

663 minimal in the winter and fall months, due to the limited energy available for ET in those months. Over
664 the warmer months, the observed and modeled ETs show distinct behaviors. CIMIS stations report two
665 peaks, one in the spring and one in the summer time. Simulated ETs, however, illustrate one peak in the
666 July. The Noah-UCM, using these parameterizations, underestimates ET rates for the most of winter and
667 spring months and overestimates them in the summer time (Fig. 4a and 4c). Including remotely sensed
668 albedo, LAI, and emissivity does not change the general seasonal pattern deviations of ET (Fig. 4a and
669 4c), but it reduces the biases considerably (with R^2=0.83 and RMSE=14.32 mm/month). We note that
670 model improvement is mostly associated with inclusion of remotely-sensed LAI maps in the model since
671 albedo and emissivity have minimal influence on latent heat fluxes from heavily vegetated pixels (see
672 Fig. 2j).
673 The new GVF and ISA values alter ET seasonal fluctuations significantly in scenario 7 (Fig. 4b). In
674 agreement with CIMIS observations, the model with inclusion of remotely sensed parameters results in
675 significantly higher ET values in the warming months (Feb.-May) and lower ETs in the summer time.
676 Noting that ISA has minimal effects over the fully vegetated pixels, one explanation for this pattern is
677 that higher green vegetation fraction detected by Landsat in late winter and early spring, increases
678 transpiration rates as soon as the required energy is available and lower measured GVFs in the summer
679 time suppresses the transpiration rates, resulting in the lower ET values. These changes enhance the
680 model performance significantly (with R^2=0.92 and RMSE= 11.77 mm/month).
681 Including all the measured parameter sets (Fig. 4d), reduces the behavioral disagreements
682 between observed and modeled monthly ET (R^2=0.86). Large biases over the summer months are also
683 reduced. However, ET values are overestimated over the rest of the year (RMSE=17.49 mm/month).
684 Although each newly developed parameter group enhances the model performance in predicting ET, the
685 advantages are countered when all of the parameters are implemented in the model. This is possibly
686 due to the complex interactions between the parameters (e.g. GVF and LAI) in the model structure.

A notable pattern detected by CIMIS data is the drop in ET values over the month of June. The sudden decrease in ET corresponds to the June Gloom weather pattern in southern California, when onshore flows result in persistent overcast skies with cool temperatures, as well as fog and drizzle in late spring and early summer [NWS, 2011]. The June Gloom effects are captured in scenarios 7 and 9 (Fig. 4b and 4d) and not seen in scenarios 1 and 8 (Fig. 4a and 4c). Since ISA has minimal influence on ET from the fully vegetated pixels and the second group fails to simulate June Gloom influence, the improvements in scenarios 7 and 9, in capturing this phenomenon, are associated with a more accurate representation of GVF.

7.2. LST Simulations

In order to further evaluate model performance and examine the impacts of different remote sensing based parameter sets, Landsat-based LST measurements are utilized (Fig. 5 and 6). Statistics (R^2 and RMSE) are also included to quantify the model performance using different urban surface parameterizations (Fig. 5). The observed LSTs, over fully vegetated pixels, are estimated with fair accuracy by the default model (R^2=0.86 and RMSE=3.21 °C; Fig 5a). The model performance has almost the same level of accuracy over low intensity residential areas and is slightly worse (<1°C) over industrial/commercial pixels (Fig. 5e). Using remote sensing data over fully vegetated and low intensity residential pixels weakly improves the biases (with <1°C improvement; Fig. 5b-d and 5f-h). Over industrial/commercial areas, a systematic underestimation of the observed LST is identified (RMSE=3.96-4.59°C; Fig. 5i-l) which seems to be persistent after using different remotely sensed parameter sets. We speculate that this underestimation of LST over highly developed areas is due to lack of representation of anthropogenic heating in the current study.

A comparison of LST at 1100 LST on 14 April 2011 with four simulation cases is also presented (Fig. 6). Alterations due to use of remote sensing products are more noticeable in this spatial examination of the results. Using all the default parameters (scenario 1), observed LST is overestimated

Deleted: is slightly worse (~1°C)

Deleted: R^2=0.62 and

Deleted: 6.15

Deleted:). Both

Deleted: groups (scenarios 7 and 8) significantly improve the correlations between the observed and simulated LSTs (RMSE of 0.76 and 0.70, respectively; Fig. 5j and 5k). When all the parameters are used (scenario 9), the RMSE is enhanced to 0.82. However, the cold biases are persistent in all simulations, more significantly over

Deleted: surfaces (Fig. 5e-l).

Deleted: Further analysis (not shown here) indicates that underestimation of LST values is due to a fundamental problem in the UCM and cannot be immediately solved with available parameter choices. This problem is discussed in a related study investigating different schemes for LST and conductive heat fluxes in the UCM [Wang et al. 2011b]. Their study shows that the current UCM formulation results in a phase lag and cold biases in simulated surface temperature when compared to observations. The discussed cold biased could potentially be resolved utilizing a spatially-analytical scheme introduced by Wang et al. [2011b].¶

over the heavily vegetated areas and underestimated over highly developed pixels (Fig. 6a and 6b). Remotely sensed GVF and ISA (in scenario 7) significantly decrease LSTs over fully vegetated and low intensity residential pixels and increase temperatures over industrial and commercial areas resulting in a better match with the observed LST map. The decreased simulated surface temperatures over heavily vegetated areas is due to higher GVF and consequently higher ET rates, which in turn lead to lower sensible heat flux and LSTs (see Fig. 3b). The increased LSTs over highly developed areas is likely due to lower GVF and higher ISA values detected in Landsat imagery, compared with the default values, which partition net radiation more into sensible heat flux (see Fig. 3b and 3f). The noticed changes in LST maps, using remotely senses albedo, LAI, and emissivity (scenario 8), are small (compare Fig. 6a and 6e). Although simulated LSTs over fully vegetated areas are decreased, the observed temperatures are still overestimated (Fig. 6f). The LST decreases in scenario 8 may be explained by evaporative cooling effect of the higher LAI values over heavily vegetated areas (see Fig. 3n). Similar to scenario 7, considerable GVF induced LST reductions, over fully vegetated areas, improve the observed LST estimations in scenario 9 (Fig. 6h). Our assessment indicates that implemented satellite derived parameter maps, particularly GVF and ISA used in scenarios 7 and 9, enhance the Noah-UCM capability to reproduce the LST differences between fully vegetated pixels and highly developed areas (simulated LST differences of 3.07, 6.78, 3.48, and 7.30 °C for scenarios 1, 7, 8, and 9 vs. observed LST difference of 11.25 °C).

7.3. Energy and Water Budget Evaluation

Differences in the simulated energy and water budgets, with different surface parameterizations (scenarios 1, 7, 8, and 9 in the Table 1) are summarized for WY 2011 (Fig. 7). The emissivity induced changes to the energy and water budgets are insignificant and not included. The illustrated radiative and turbulent heat fluxes show that, unlike the longwave radiative fluxes, the simulated available solar radiations are altered considerably using different urban parameter sets (up to %6), particularly over fully vegetated (Fig. 7a) and industrial/commercial pixels (Fig. 7c). These changes are induced by new

Deleted: result

Deleted: However the model still underestimates the observed LSTs over the industrial and commercial pixels (Fig. 6b and 6e).

Deleted: 1.31, 4.81, 1.55

Deleted: 4.93

Deleted: Nevertheless, the model still underestimates remotely sensed LST values, by about 9.91 °C for scenario 9, over the highly developed areas.

Deleted: Regardless of the parameterization processes, cold biases are persistent in all simulations, particularly over high intensity residential and industrial/commercial pixels (Fig. 6). As explained above, this underestimation of LST values is consistent with the literature and is reported to be due to a fundamental problem in the UCM which produces a phase lag and cold biases in simulated LST [Wang et al., 2011b].¶

surface albedo values utilized in scenarios 8 and 9. It is also observed that most of the incoming radiative energy is dissipated through latent heat fluxes, over heavily vegetated pixels (Fig. 7a and 7b), and sensible heat fluxes over industrial/commercial areas (Fig. 7c). These turbulent fluxes are also altered when different surface parameterizations are incorporated. Implementing all the remotely sensed parameters (scenario 9), the annual latent heat flux is increased (12%) over fully vegetated pixels (Fig. 7a), and the annual sensible heat flux is decreased (32%) over industrial/commercial pixels (Fig. 7c). Ground heat fluxes, however, are insignificant and unchanged.

Water budget terms also show variable behavior using different parameter sets over different land cover types (Fig. 7 d-f). Annual irrigation amounts exceed received precipitations over the pixels with significant vegetation fractions (Fig. 7d and 7e). This pattern is not rare in semi-arid regions [CDWR 1975, Mini et al., 2014]. In these areas, most of incoming water is lost through ET (Fig. 7d and 7e). Areas with high coverage of impervious surfaces, however, dissipate most of the incoming moisture through surface runoff (Fig. 7f). The alterations in the annual ET rates are, for the most part, due to the changes in the GVF parameterizations (scenarios 7 and 9; Fig. 7d-f). Sub-surface runoff annual rates, on the other hand, are altered using new ISA values (scenarios 7 and 9; Fig. 7e and 7f). Changes in the annual ET values are as large as 145, 156, and 79.4 mm over fully vegetated, low intensity residential and industrial/commercial pixels, respectively (Fig. 7d-f).

To further verify the capability of Noah-UCM to reproduce observed ET quantities, additional evaluation of the model is conducted utilizing ground-based chamber ET measurements in the greater Los Angeles area [Moering, 2011]. Instantaneous ET measurements, over an irrigated park in the study domain during WY 2011, are converted to daily and then annual ET estimates (1224 mm) and compared with the simulated ET values over the parks (Fig. 7d). As expected, the observed ET is best reproduced by scenario 7 (Bias of 1.47 mm) due to more accurate representation of GVF in the model. Scenarios 1 (with the default parameters) and 8 underestimate, with biases of 58.65 and 65.32 mm, respectively.

794 Scenario 9, with all the remotely sensed parameters, overestimates the measured ET (with bias of 86.24
795 mm). These shortcomings are likely due to: (1) a lack of accurate representation of GVF in the default
796 parameter sets, used in scenarios 1 and 8, (2) the uncertainties associated with the estimated LAI values
797 utilized in scenarios 8 and 9, and (3) complex interactions between GVF and LAI noted in scenario 9.
798 The presented analysis of energy balance (Fig. 7) suggests that GVF, albedo and LAI play an important
799 role in regulating simulated radiative energy budget and turbulent fluxes, mainly by affecting the
800 available net radiation and transpiration quantities. GVF, ISA, and LAI also alter the study area
801 transpiration and ET values, as well as surface runoff rates.
802
803 **8. Conclusions**
804 In the current work we investigate the utility of a select set of remote sensing based surface parameters
805 in the Noah-UCM modeling framework over a highly developed urban area. It was found that remote
806 sensing data show significantly different magnitudes and seasonal patterns of GVF when compared with
807 the default values. The reason for this mismatch is the significant and year round irrigation in the Los
808 Angeles area which is not accounted for in the default parameter tables. Irrigated landscapes maintain
809 constant greenness rather than a seasonal behavior of greening in the winter/spring and browning in
810 the summer. The noticed differences between the monthly LAI values from default tables and remotely
811 sensed data are also due to complex irrigation patterns. Another factor that contributes to this
812 mismatch is the fact that landscape plantings are quite different from agricultural crops due to their
813 being composed of collections of vegetation species which is not taken into account in the vegetation
814 parameter tables in the Noah LSM [CDWR, 2000; Vahmani and Hogue, 2013; 2014]. There are also
815 considerable deviations between the look-up-table-based ISA, albedo and emissivity maps and the
816 remotely sensed values. The results of our analysis agree with previous studies which show high
817 sensitivity of the Noah-UCM to GVF, ISA, albedo, and LAI, and minimal model sensitivity to emissivity

[Loridan et al., 2010; Wang et al., 2011]. Our results show that GVF, ISA and LAI are critical in the simulations of latent and sensible heat flux, and that albedo plays a key role in the sensible heat flux simulations.

Our assessment of the Noah-UCM ET estimation shows that using the default parameters leads to significant errors in the model predictions of monthly ET fields (RMSE= 22.06 mm/month) over the study domain in Los Angeles. Results show that accurate representation of GVF is critical to reproduce observed ET patterns over vegetated areas in the urban domains. LAI also plays an important role in ET simulations. However, simulations incorporating the remotely sensed GVF values outperform (RMSE= 11.77 mm/month) simulations with the new LAI estimates (RMSE=14.32 mm/month). This could be due to several reasons. First, there are uncertainties associated with the remote sensing based LAI retrieval, including non-linearity of LAI-vegetation index (RSR) relationships [Latifi and Galos, 2010], which do not apply to NDVI-based GVF. Second, more accurate representation of GVF values in the Noah-UCM not only improves the assigned LAI values to the vegetated pixels in the model but also enhances other parameters inputs as well (i.e. albedo, emissivity, and roughness length). Further analysis of the model performance indicates that implemented satellite derived parameter maps, particularly GVF and ISA, enhance the Noah-UCM capability to reproduce the LST differences between fully vegetated pixels and highly developed areas (simulated LST differences of 3.07 and 6.78 °C for scenarios with default and remotely sensed GVF and ISA vs. observed LST difference of 11.25 °C).

Our analysis of energy balance suggests that GVF, albedo and LAI play an important role in regulating simulated radiative energy budget and turbulent fluxes, mainly by affecting the available net radiation and ET quantities. With regard to urban water balance, GVF, ISA, and LAI play a key role in surface hydrologic fluxes, including ET and surface runoff. When compared with in-situ observations, Noah-UCM shows the capacity to reproduce ET fields with relatively high accuracy (Bias of 1.47 mm) when GVF maps are updated using remote sensing data.

Deleted: 1.31

Deleted: 4.81

Deleted: Nevertheless, the model still underestimates remotely sensed LST values, over highly developed areas. We speculate that the underestimation of LST values, particularly over high intensity residential and industrial/commercial areas, is due to structural parameterization in the UCM and cannot be immediately solved with available parameter choices.

In summary, the current study highlights the significant deviations between the spatial distributions and seasonal fluctuations of the default and remotely sensed parameter sets in the Noah-UCM. We illustrate that replacing default parameters with the measured values reduces significant biases in model predictions of the surface fluxes within irrigated urban areas. This ultimately has key implications in feedback processes to the atmosphere when the Noah-UCM is coupled with the widely used WRF model, which has been increasingly applied over urban areas to examine the exchange of heat, moisture, momentum or pollutants. Semi-arid urban cities, in particular, are receiving much attention in the literature, given their accelerated growth and increasing dependence on external water sources. More accurate representation of both water and energy fluxes in commonly used modeling frameworks is critical for regional resource management as well as predictions of urban processes under future climate conditions. Although this study focuses on the widely used single layer UCM, we speculate that implementation of the more accurate remote sensing based parameters (particularly, GVF and ISA) may also enhance performance of the Noah-BEP [Martilli et al., 2002], which is currently the most sophisticated urban scheme in WRF. In this multi-layer UCM a similar approach to the single layer UCM is used based on an urban fraction (or ISA) parameter that couples the Noah outputs over pervious portion of pixels and UCM outputs over developed surfaces.

Acknowledgements

Funding for this research was supported by an NSF Hydrologic Sciences Program CAREER Grant (#EAR0846662), a 2012 NASA Earth and Space Science Fellowship (#NNX12AN63H), and an NSF Water Sustainability and Climate (WSC) grant (#EAR12040235).

871 **References**

872 Arnfield, A. J.: Two decades of urban climate research: A review of turbulence, exchanges of energy and
873 water, and the urban heat island, Int. J. Climatol., 23: 1–26, doi: 10.1002/joc.859, 2003.

874 Artis, D. A. and Carnahan, W. H.: Survey of emissivity variability in thermography of urban areas, Remote
875 Sensing of Environment, 12, 313–329, 1982.

876 Bauer, M. E., Loeffelholz, B., and Wilson, B.: Estimating and mapping impervious surface area by
877 regression analysis of Landsat imagery, Remote Sensing of Impervious Surfaces, pp. 3−20, Boca Raton,
878 Florida: CRC Press, 2007.

879 Bornstein, R.: Urban climate models: Nature, limitations, and applications, Meteorol. Atmos. Phys., 38,
880 185–194, 1987.

881 Burian, S. , Brown, M. J., Augustus, N.: Development and assessment of the second generation National
882 Building Statistics database, Seventh Symposium on the Urban Environment, San Diego, CA, 10–13
883 September, American Meteorological Society: Boston, MA, Paper 5.4, 2007.

884 Burian, S. J., Stetson, S. W., Han, W., Ching, J., and Byun, D.: High resolution dataset of urban canopy
885 parameters for Houston, Texas, Preprint proceedings, Fifth Symposium on the Urban Environment,
886 Vancouver, BC, Canada, 23–26 August, American Meteorological Society: Boston, MA, 2004.

887 Burian, S., Brown, M., McPherson, T. N., Hartman, J., Han, W., Jeyachandran, I., Rush, J.: Emerging urban
888 databases for meteorological and dispersion, Sixth Symposium on the Urban Environment, Atlanta, GA,
889 28 January–2 February, American Meteorological Society: Boston, MA, Paper 5.2, 2006.

Deleted: 9,

California Department of Water Resources (CDWR): A guide to estimating irrigation water needs of landscape plantings in California: The landscape coefficient method and WUCOLS III, Department of Water resources, State of California, 1–150, 2000.

California Department of Water Resources (CDWR): California's ground water, bulletin 118, Department of Water resources, State of California, 1975.

Changnon, S. A. and Huff, F. A.: The urban-related nocturnal rainfall anomaly at St. Louis, J. Climate Appl. Meteor., 25, 1985–1995, doi:10.1175/1520-25 0450(1986)025<1985:TURNRA>2.0.CO;2, 1986.

Changnon, S. A.: Inadvertent weather modification in urban area: Lessons for global climate change. Bull. Amer. Meteor. Soc., 73, 619–627, doi:10.1175/1520-0477(1992)073<0619:IWMIUA>2.0.CO;2, 1992.

Chen, F. and Dudhia, J.: Coupling an advanced land-surface/hydrology model with the Penn State/NCAR MM5 modeling system. Part I: model implementation and sensitivity, Monthly Weather Review, 129: 569–585, 2001.

Chen, F., Janjic, Z., and Mitchell, K.: Impact of atmospheric surface layer parameterization in the new land-surface scheme of the NCEP mesoscale Eta model, Boundary-Layer Meteorology, 85: 391–421, DOI:10.1023/A:1000531001463, 1997.

Chen, F., Kusaka, H., Bornstein, R., Ching, J., Grimmond, C. S. B., Grossman-Clarke, S., Loridan, T., Manning, K. W., Martilli, A., Miao, S., Sailor, D., Salamanca, F. P., Taha, H., Tewari, M., Wang, X., Wyszogrodzki, A. A., and Zhang, C.: The integrated WRF/urban modelling system: development, evaluation, and applications to urban environmental problems, Int. J. Climatol., 31: 273–288. doi: 10.1002/joc.2158, 2011.

Deleted: http://dx.doi.org/

Deleted: http://dx.doi.org/

914 Chen, F., Kusaka, H., Tewari, M., Bao, J. W., Harakuchi, H.: Utilizing the coupled WRF/LSM/urban
915 modeling system with detailed urban classification to simulate the urban heat island phenomena over
916 the Greater Houston area, Paper 9.11, American Meteorological Society Fifth Symposium on the Urban
917 Environment, Vancouver, BC, Canada, 2004.

918 Chen, F., Mitchell, K., Schaake, J., Xue, Y., Pan, H.-L., Koren, V., Duan, Q. Y., Ek, M., Betts, A.: Modeling of
919 land-surface evaporation by four schemes and comparison with FIFE observations, J. Geophys. Res.,
920 101(D3), 7251–7268, doi:10.1029/95JD02165, 1996.

921 Cheng, F. Y. and Byun, D.W.: Application of High Resolution Land Use and Land Cover Data for
922 Atmospheric Modeling in the Houston-Galveston Metropolitan Area: Part I, Meteorological Simulation
923 Results, Atmospheric Environment, 42, 7795-7811, doi:10.1016/j.atmosenv.2008.04.055, 2008.

924 Cheng, F. Y., Hsu, Y. C., Lin, P. L., Lin, T. H.: Investigation of the Effects of Different Land Use and Land
925 Cover Patterns on Mesoscale Meteorological Simulations in the Taiwan Area, J. Appl. Meteor. Climatol.,
926 52, 570–587, doi: http://dx.doi.org/10.1175/JAMC-D-12-0109.1, 2013.

927 Ching, J., Brown, M., McPherson, T., Burian, S., Chen, F., Cionco, R., Hanna, A., Hultgren, T., Sailor, D.,
928 Taha, H., Williams, D.: National Urban Database and Access Portal Tool, NUDAPT, Bulletin of the
929 American Meteorological Society, 90(8): 1157–1168, DOI:10.1175/2009BAMS2675.1, 2009.

930 Cotton, W. R. and Pielke, R. A.: Human impacts on weather and climate. Cambridge: Cambridge
931 University Press, 1995.

932 De Ridder, K., Bertrand, C., Casanova, G., and Lefebvre, W.: Exploring a new method for the retrieval of
933 urban thermophysical properties using thermal infrared remote sensing and deterministic modeling, J.
934 Geophys. Res., 117, D17108, doi:10.1029/2011JD017194, 2012.

935 Ek, M. B., Mitchell, K. E., Lin, Y., Rogers, E., Grunmann, P., Koren, V., Gayno, G., Tarpley, J. D.:
936 Implementation of Noah land surface model advances in the National Center for Environmental
937 Prediction operational mesoscale Eta model , J. Geophys. Res., 108, 8851, doi:10.1029/2002JD003296,
938 2003.

939 Giannaros, T. M., Melas, D., Daglis, I. A., Keramitsoglou, I., Kourtidis, K.: Numerical study of the urban
940 heat island over Athens (Greece) with the WRF model, Atmospheric Environment, Volume 73, 103-111,
941 doi:10.1016/j.atmosenv.2013.02.055, 2013.

942 Gutman, G. and Ignatov, A.: Derivation of green vegetation fraction from NOAA/AVHRR for use in
943 numerical weather prediction models, Int. J. Remote Sens., 19: 1533-1543, 1998.

944 Hanasaki, N., Kanae, S., Oki, T., Masuda, K., Motoya, K., Shirakawa, N., Shen, Y., and Tanaka, K.: An
945 integrated model for the assessment of global water resources- Part 1: Model description and input
946 meteorological forcing, Hydrol. Earth Syst. Sci., 12, 1007-1025, doi:10.5194/hess-12-1007-2008, 2008a.

947 Hanasaki, N., Kanae, S., Oki, T., Masuda, K., Motoya, K., Shirakawa, N., Shen, Y., and Tanaka, K.: An
948 integrated model for the assessment of global water resources- Part 2: Applications and assessments,
949 Hydrol. Earth Syst. Sci., 12, 1027-1037, doi:10.5194/hess-12-1027-2008, 2008b.

950 Jiang, X., Wiedinmyer, C., Chen, F., Yang, Z. L., and Lo, J. C. F.: Predicted impacts of climate and land use
951 change on surface ozone in the Houston, Texas, area, J. Geophys. Res., 113, D20312,
952 doi:10.1029/2008JD009820, 2008.

953 Jin, M. and Shepherd J. M.: Inclusion of urban landscape in a climate model—How can satellite data
954 help?, Bull. Am. Meteorol. Soc., 86(5), 681–689, DOI:10.1175/BAMS-86-5-681, 2005.

955 Johnson, T. D. and Belitz K.: A remote sensing approach for estimating 1 the location and rate of urban
956 irrigation in semi-arid climates, Journal of Hydrology, 414-415, 86-98, 2012.

957 Justice, C. O., Townshend, J. R. G., Vermote, E. F., Masuoka, E., Wolfe, R. E., Saleous, N., Roy, D. P.,
958 Morisette, J. T.: An overview of MODIS land data processing and product status. Remote Sensing of
959 Environment, 83(1–2), 3–15, 2002.

960 Kalnay, E. and Cai, M.: Impact of urbanization and land-use change on climate, Nature, 423(29),
961 528−531, 2003.

962 Kusaka, H., Kimura, F.: Thermal effects of urban canyon structure on the nocturnal heat island:Numerical
963 experiment using a mesoscale model coupled with an urban canopy model, J. Appl. Meteorol. 43: 1899–
964 1910, 2004.

965 Kusaka, H., Kondo, H., Kikegawa, Y., and Kimura, F.: A simple single-layer urban canopy model for
966 atmospheric models: Comparison with multi-layer and slab models, Bound.-Layer Meteor., 101, 329–
967 358, 2001.

968 Landsberg, H. E.: The urban climate. New York: Academic Press, 1981.

969 Latifi, H. and Galos, B.: Remote sensing-supported vegetation parameters for regional climate models: a
970 brief review, iForest 3: 98-101, doi: 10.3832/ifor0543-003, 2010.

971 Loridan, T., Grimmond, C. S. B., Grossman-Clarke, S., Chen, F., Tewari, M., Manning, K., Martilli, A.,
972 Kusaka, H., Best, M.: Trade-offs and responsiveness of the single-layer urban parameterization in WRF:
973 an offline evaluation using the MOSCEM optimization algorithm and field observations, Q.J.R. Meteorol.
974 Soc., 136: 997–1019. doi: 10.1002/qj.614, 2010.

975 Lowry, W.: Urban effects on precipitation amount, Progress in Physical Geography, 22(4), 477−520, DOI:
976 10.1177/030913339802200403, 1998.

977 Marshall, C. H., Pielke, R. A., Steyaert, L., and Willard, D.: The impact of anthropogenic land-cover
978 change on the Florida peninsula sea breezes and warm season sensible weather, Mon. Wea. Rev., 132,
979 28–52, doi: http://dx.doi.org/10.1175/1520-0493, 2004.

980 Martilli, A, Clappier, A, and Rotach, M. W.: An urban surface exchange parameterization for mesoscale
981 models, Boundary-Layer Meteorology 104: 261–304, 2002.

982 McPherson, E. G., Simpson, J. R., Xiao, Q., Wu, C.: Los Angeles 1-million tree canopy cover assessment,
983 Gen. Tech. Rep. PSW-GTR-207, Albany, CA: U.S. Department of Agriculture, Forest Service, Pacific
984 Southwest Research Station, 52 p, 2008.

985 Miao, S. and Chen F.: Formation of horizontal convective rolls in urban areas, Atmospheric Research,
986 89(3): 298–304, doi:10.1016/j.atmosres.2008.02.013, 2008.

987 Miao, S., Chen F., LeMone, M. A., Tewari M., Li, Q., Wang, Y.: An observational and modeling study of
988 characteristics of urban heat island and boundary layer structures in Beijing, J. Appl. Meteor. Climatol.,
989 48, 484–501, doi: http://dx.doi.org/10.1175/2008JAMC1909.1, 2009.

990 Mini, C., Hogue, T. S., and Pincetl, S.: Estimation of Residential Outdoor Water Use in Los Angeles,
991 California, Landscape Urban Plan, 127, 124–135, doi:10.1016/j.landurbplan.2014.04.007, 2014.

992 Moering, D. C.: A comparative study of evapotranspiration rates between irrigated and non-irrigated
993 parks in Los Angeles, M.S. thesis, Dep. of Civil and Env. Eng., Univ. of California Los Angeles, Los Angeles,
994 California, 2011.

995 National Oceanographic and Atmospheric Administration-Coastal Services Center (NOAA-CSC): Southern
996 California 2000-Era Land Cover/Land Use, LANDSAT-TM, 10m, NOAA-CSC, Charleston, SC, 2003.

Deleted: ., 2014:

Deleted: and Urban Planning (in press)

National Weather Service (NWS): Jet Stream - The Marine Layer, NOAA National Weather Service, http://www.srh.noaa.gov/jetstream/ocean/marine.htm (last access: 24 February 2013), 2011.

Niyogi, D., Holt, T., Zhong, S., Pyle, P. C., and Basara, J.: Urban and land surface effects on the 30 July 2003 mesoscale convective system event observed in the Southern Great Plains, J. Geophys. Res., 111, D19107, doi:10.1029/2005JD006746, 2006.

Pielke, R. A. Sr., Marland, G., Betts, R. A., Chase, T. N., Eastman, J. L., Niles, J. O., Niyogi, D., and Running, S.: The influence of land-use change and landscape dynamics on the climate system: Relevance to climate change policy beyond the radiative effect of greenhouse gases, Phil. Trans. R. Soc. London A, 360(Special Theme Issue), 1705–1719, 2002.

Pokhrel, Y., Hanasaki, N., Koirala, S., Cho, J., Kim, H., Yeh, P. J.-F., Kanae, S., and Oki, T.: Incorporating anthropogenic water regulation modules into a land surface model, Journal of Hydrometeorology, 13 (1), 255-269, doi: 10.1175/JHM-D-11-013.1, 2012.

Sailor, D. J., Lu, L.: A top-down methodology for developing diurnal and seasonal anthropogenic heating profiles for urban areas, Atmospheric Environment 38: 2737–2748, doi:10.1016/j.atmosenv.2004.01.034, 2004.

Schaaf, C. B., Gao, F., Strahler, A. H., Lucht, W., Li, X. W., Tsang, T., Strugnell, N. C., Zhang, X. Y., Jin, Y. F., Muller, J. P., Lewis, P., Barnsley, M., Hobson, P., Disney, M., Roberts, G., Dunderdale, M., Doll, C., d'Entremont, R. P., Hu, B. X., Liang, S. L., Privette, J. L., Roy, D.: First operational BRDF, albedo nadir reflectance products from MODIS, Remote Sensing of Environment, 83(2-Jan), 135-148, 2002.

Shuai, Y., Masek, J. G., Gao, F., and Schaaf, C. B.: An algorithm for the retrieval of 30-m snow-free albedo from Landsat surface reflectance and MODIS BRDF, Remote Sensing of Environment, 115, 2204-2216, doi:10.1016/j.rse.2011.04.019, 2011.

Deleted: ,

Shuai, Y., Schaaf, C. B., Strahler, A. H., Liu, J., and Jiao, Z.: Quality assessment of BRDF/albedo retrievals in MODIS operational system, Geophysical Research Letters, 35, L05407, 5PP, doi:10.1029/2007GL032568, 2008.

Sobrino, J. A. and Raissouni, N.: Toward remote sensing methods for land cover dynamic monitoring: Application to Morocco, International Journal of Remote Sensing, 21, pp. 353–366 DOI:10.1080/014311600210876, 2000.

Sobrino, J. A., Raissouni, N., and Li, Z. L.: A comparative study of land surface emissivity retrieval from NOAA data. Remote Sensing of Environment, 75, pp. 256–266, 2001.

Song, M. and Civco, D. L.: A knowledge-based approach for reducing cloud and shadow, Proceedings of the American Society of Photogrammetry and Remote Sensing annual convention, Washington, DC: American Society of Photogrammetry and Remote Sensing, 7 p, 2002.

State of California Department of Water Resources (SCDWR): California irrigation management information system, Sacramento, CA: State of California Department of Water Resources, Available at: http://www.water.ca.gov/, 2009.

Stathopoulou, M. and Cartalis, C.: Daytime urban heat islands from Landsat ETM+ and Corine land cover data: An application to major cities in Greece, Solar Energy, 81 (3), pp. 358-368, doi:10.1016/j.solener.2006.06.014, 2007.

Stathopoulou, M., Cartalis, C., and Petrakis, M.: Integrating Corine Land Cover data and Landsat TM for surface emissivity definition: application to the urban area of Athens, Greece, International Journal of Remote Sensing, 28:15, 3291-3304, DOI:10.1080/01431160600993421, 2007.

Stenberg, P., Rautiainen, M., Manninen, T., Voipio, P., and Smolander, H.: Reduced simple ratio better than NDVI for estimating LAI in Finnish pine and spruce stands, Silva Fennica 38(1): 3–14, 2004.

Taha, H., Ching, J. K. S.: UCP/MM5 Modeling in conjunction with NUDAPT: model requirements, updates, and applications, Seventh Symposium on the Urban Environment, San Diego, CA, 10–13 September, American Meteorological Society: Boston, MA, Paper 6.4, 2007.

Taha, H., Douglas, S., and Haney, J.: Mesoscale meteorological and air quality impacts of increased urban albedo and vegetation, Energy and Buildings, 25, 169−177, DOI: 10.1016/S0378-7788(96)01006-7, 1997.

Taha, H.: Meso-urban meteorological and photochemical modeling of heat island mitigation, Atmospheric Environment, 42: 8795–8809, DOI:10.1016/j.atmosenv.2008.06.036, 2008.

Taha, H.: Modifying a mesoscale meteorological model to better incorporate urban heat storage: a bulk-parameterization approach, J. Appl. Meteorol., 38, 466–473, doi:10.1175/1520-0450(1999)038<0466:MAMMMT>2.0.CO;2, 1999.

Tan, M. and Li, X.: Integrated assessment of the cool island intensity of green spaces in the mega city of Beijing, International Journal of Remote Sensing, 34:8, 3028-3043, DOI: 10.1080/01431161.2012.757377, 2013.

Tewari, M., Kusaka, H., Chen, F., Coirier, W. J., Kim, S., Wyszogrodzki, A., Warner, T. T.: Impact of coupling a microscale computational fluid dynamics model with a mesoscale model on urban scale contaminant transport and dispersion, Atmospheric Research 96: 656–664, doi:10.1016/j.atmosres.2010.01.006, 2010.

US Census: US Census Bureau Releases Data on Population Distribution and Change in the US Based on Analysis of 2010 Census Results, US Census Bureau, 24 March 2011.

Vahmani, P. and Hogue, T. S.: Modelling and analysis of the impact of urban irrigation on land surface fluxes in the Los Angeles metropolitan area, Climate and Land Surface Changes in Hydrology Proceedings of H01, IAHS-IAPSO-IASPEI Assembly, Gothenburg, Sweden, July 2013, IAHS Publ. 359, 2013.

Deleted: Meteor

Deleted: http://dx.doi.org/

Deleted: U.S.

Deleted: U.S.

Deleted: U.S.

Deleted: U.S.

Deleted: 24,

Vahmani, P. and Hogue, T. S.: Incorporating an Urban Irrigation Module into the Noah Land Surface Model Coupled with an Urban Canopy Model, J. Hydrometeorol., doi:10.1175/JHMD-13-0121.1, in press, 2014.

Van Wevenberg, K., De Ridder, K., Van Rompaey, A.: Modeling the contribution of the Brussels heat island to a long temperature time series, Journal of Applied Meteorology and Climatology, 47, 976e990, DOI: 10.1175/2007JAMC1482.1, 2008.

Wang, X. M., Chen, F., Wu, Z. Y., Zhang, M. G., Tewari, M., Guenther, A., and Wiedinmyer, C.: Impacts of weather conditions modified by urban expansion on surface ozone: comparison between the Pearl River Delta and Yangtze River Delta regions, Adv. Atmos. Sci, 26(5), 962-972, doi: 10.1007/s00376-009-8001-2, 2009.

Wang, Z. H., Bou-Zeid, E., Au, S. K., and Smith, J. A.: Analyzing the sensitivity of WRF's single-layer urban canopy model to parameter uncertainty using advanced Monte Carlo simulation, J. Appl. Meteor. Climatol., 50, 1795–1814, doi: http://dx.doi.org/10.1175/2011JAMC2685.1, 2011.

Wei-guang, M., Yan-xia, Z., Jiang-nan, L., Wen-shi, L., Guang-feng, D., and Hao-rui, L.: Application of WRF/UCM in the simulation of a heat wave event and urban heat island around Guangzhou, Journal of Tropical Meteorology, 03, 257-267, doi: 10.3969/j.issn.1006-8775.2011.03.007, 2011.

Deleted: Journal of Hydrometeorology, 2014 (in press).

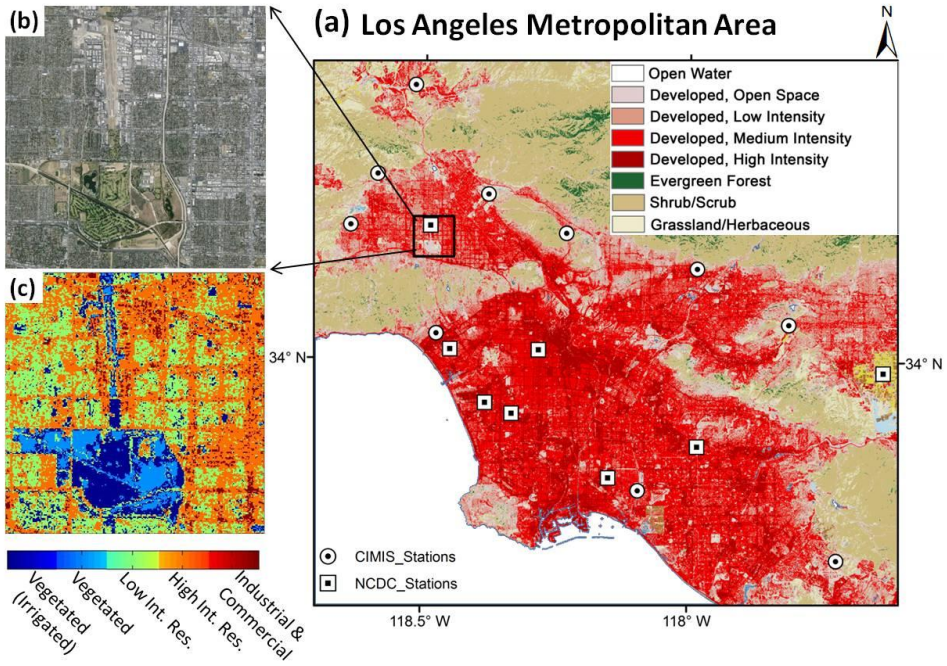

Figure 1. (a) NOAA C-CAP Land cover map of the Los Angeles metropolitan area including study domain, 10 CIMIS stations (white circles), and 8 NCDC stations (white squares), (b) Google image of the study domain, and (c) The Noah/UCM urban land cover classification of the study domain.

Deleted: 1

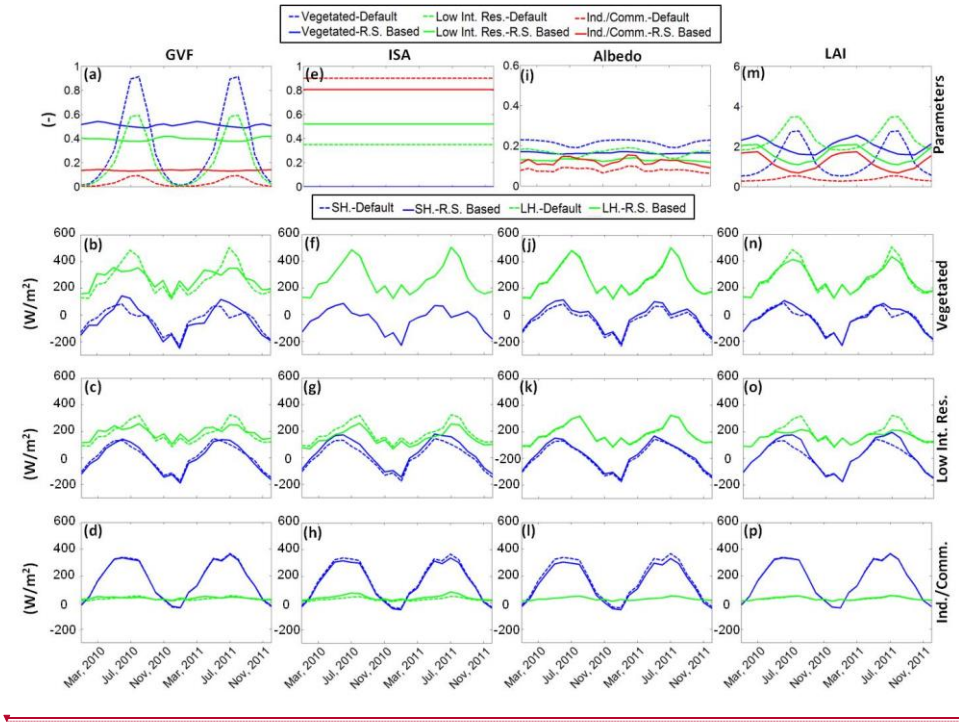

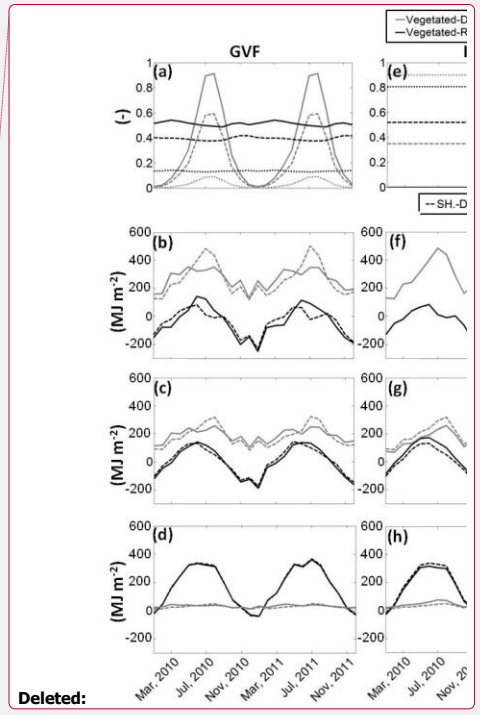

Deleted:

Figure 2. Monthly time series of default Noah/UCM compared with remote sensing based GVF, ISA, albedo, and LAI (row 1) and modeled cumulative monthly sensible and latent heat fluxes (MJ m^{-2}) over fully vegetated (row 2), low intensity residential (row 3) and industrial/commercial areas (row 4) using the default and newly estimated parameters: (b-d) GVF, (f-h) ISA, (j-l) albedo, and (n-p) LAI.

Deleted: 2

Deleted: a,e, i, and m

Deleted: ,

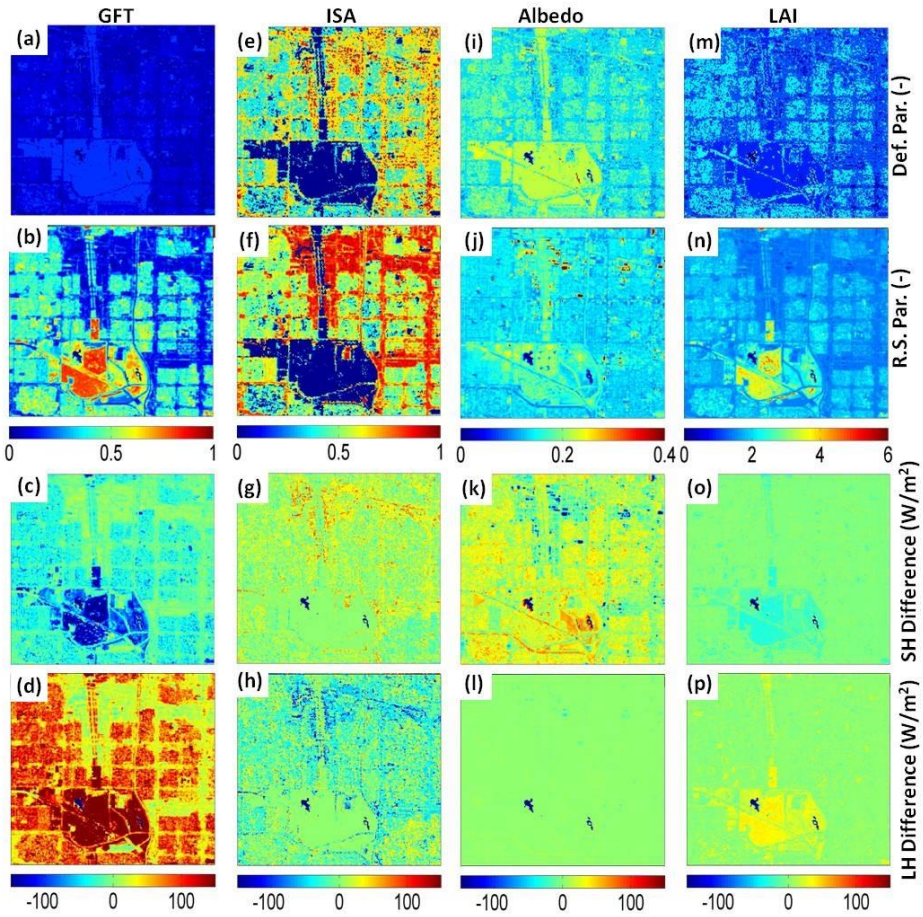

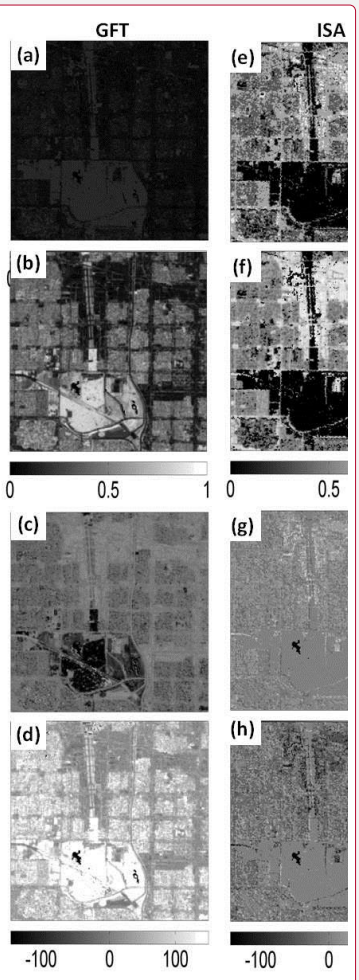

Figure 3. Spatial distributions of GVF, ISA, albedo, and LAI based on Noah/UCM lookup tables (row 1) compared with remotely sensed values (row 2) and simulated difference maps of sensible (row 3) and latent (row 4) heat fluxes using default and remotely sensed urban surface parameters: (c and d) GVF, (g and h) ISA, (k and l) albedo, and (o and p) LAI. Valid at 1100 LST on 14 April 2011.

Deleted:

Deleted: 3

Deleted: remote sensing based

Deleted: (a, e, i, and m) compared with those

Deleted: b, f, j, and n

Deleted: turbulent

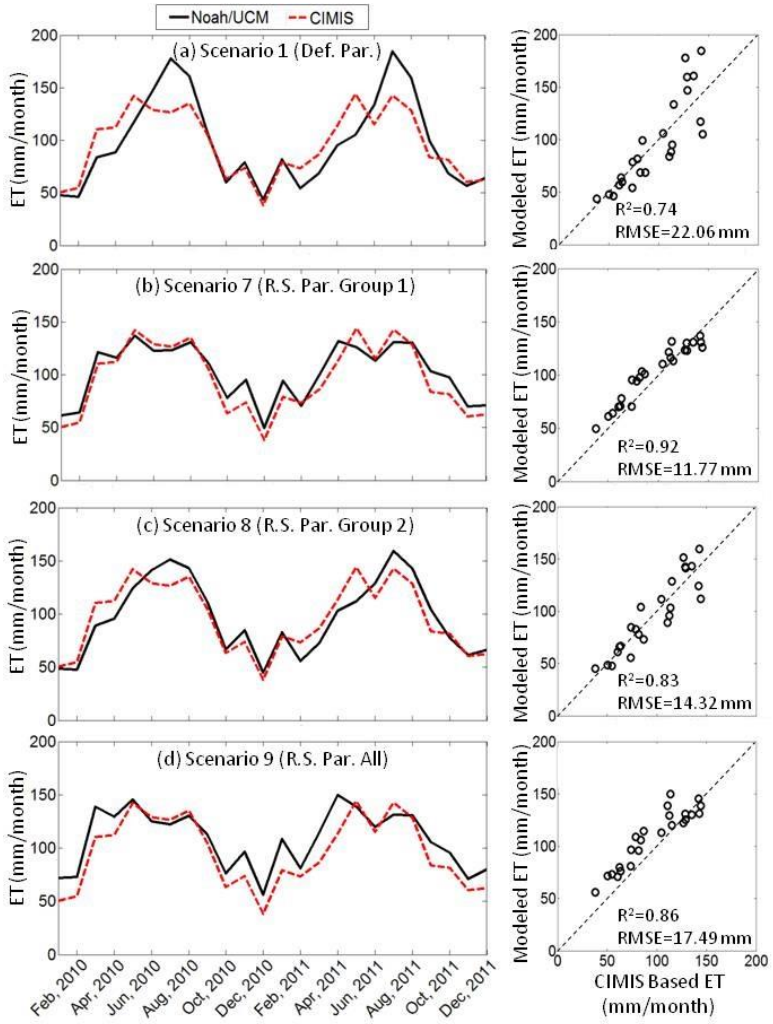

Figure 4. Noah/UCM simulated cumulative monthly ET, averaged over fully vegetated pixels using different urban surface parameterizations: scenarios (a) 1, (b) 7, (c) 8, and (d) 9 in the table 1 and their comparisons with CIMIS-based ET measurements spanning 2010 and 2011. Scatter plots of these comparisons are also included (right).

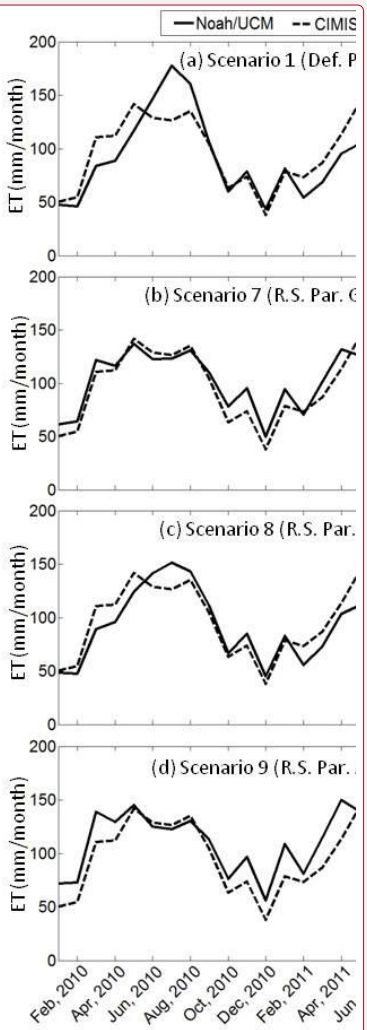

Deleted:

Deleted: 4

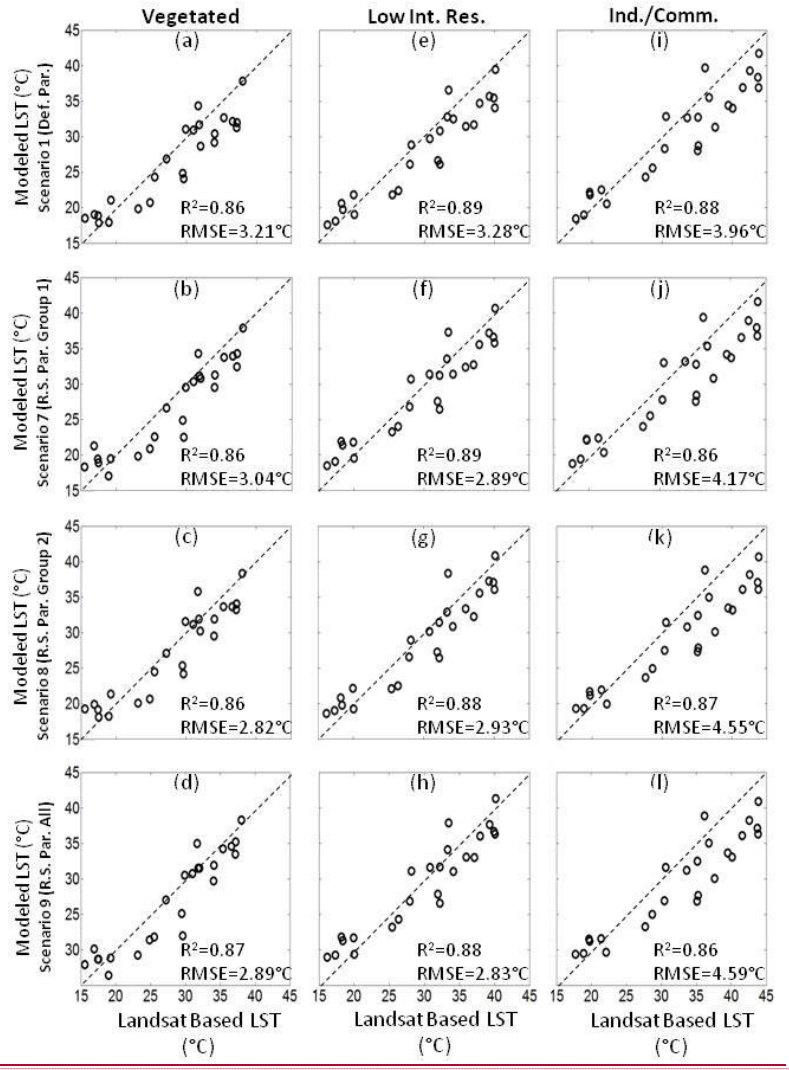

Figure 5. Scatter plots of observed (Landsat-based) versus simulated LSTs averaged over different land cover types using different urban surface parameterizations, including scenarios 1 (first row), 7 (second row), 8 (third row), and 9 (forth row) in Table 1.

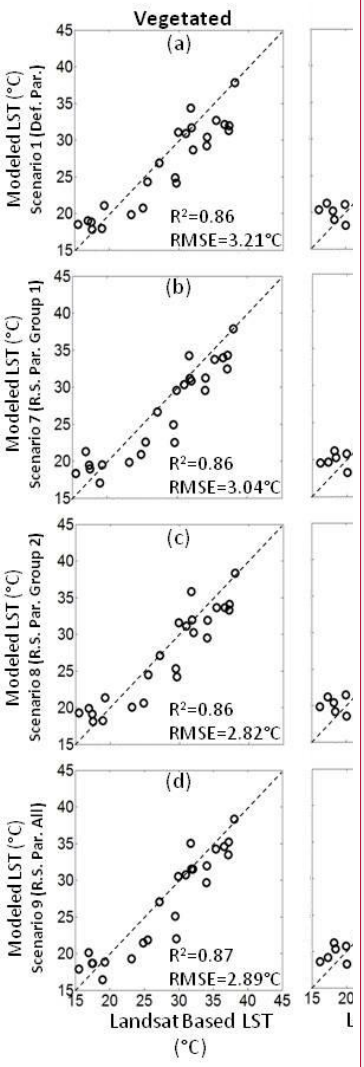

Deleted:

Deleted:

Deleted: 5

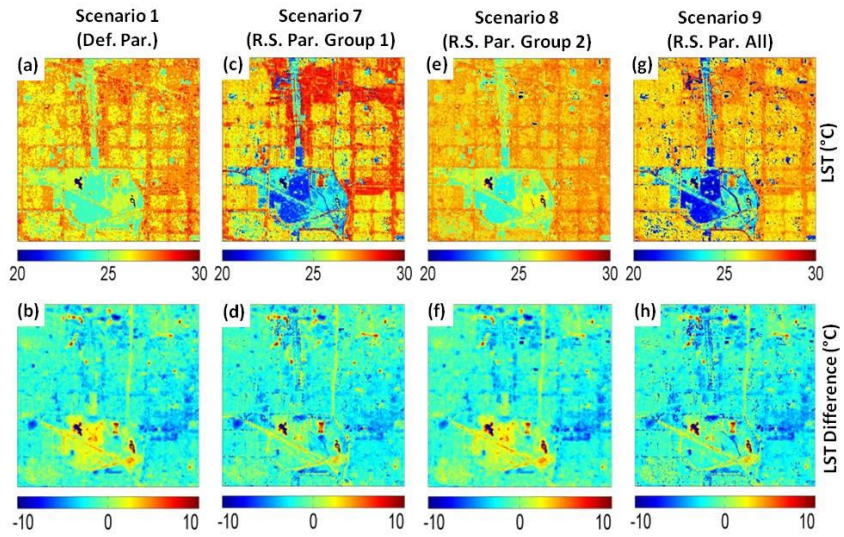

Figure 6. Noah/UCM simulated LST maps using different urban surface parameterizations: scenarios 1, 7, 8, and 9 from Table 1 (top row) as well as differences between simulated and observed land surface temperature at 1100 LST on 14 April 2011 (bottom row).

Deleted:

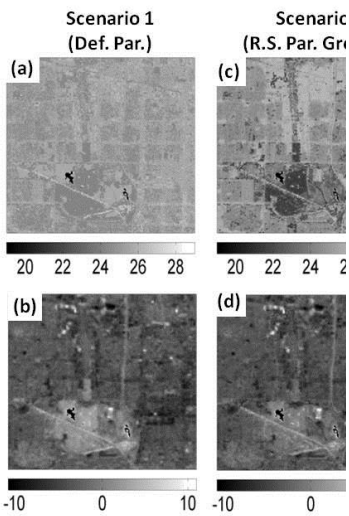

Deleted:

Deleted: 6

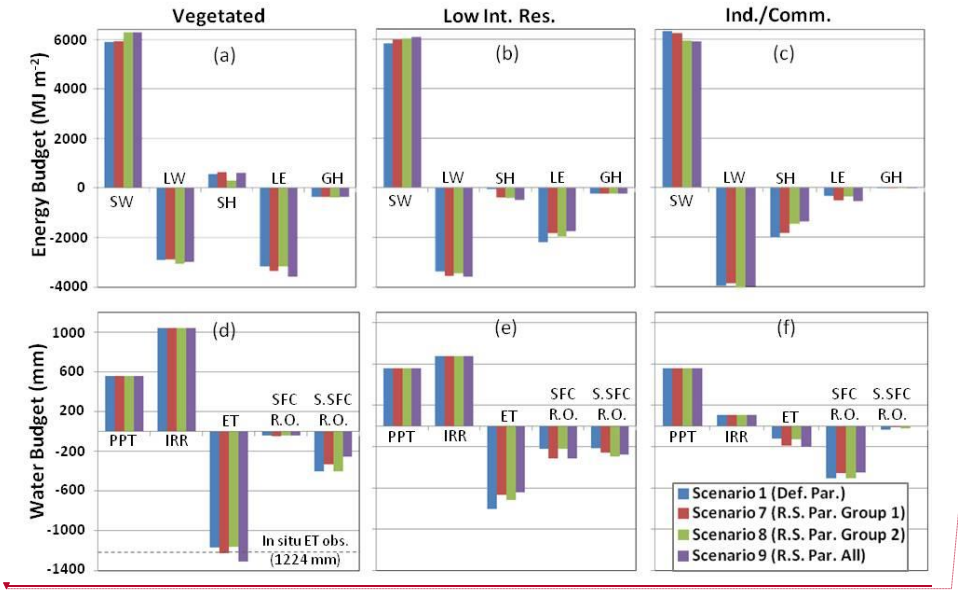

Figure 7. Differences in simulated energy (top) and water (bottom) budgets for WY 2011, using different urban surface parameterization and averaged over different land cover types. Energy budget terms include: shortwave radiation (SW), longwave radiation (LW), and sensible (SH), latent (LH), and ground (GH) heat fluxes. Water budget terms include: precipitation (PPT), irrigation water (IRR), evapotranspiration (ET), surface runoff (SFC R.O.), and sub-surface runoff (S.SFC R.O.).

Deleted:

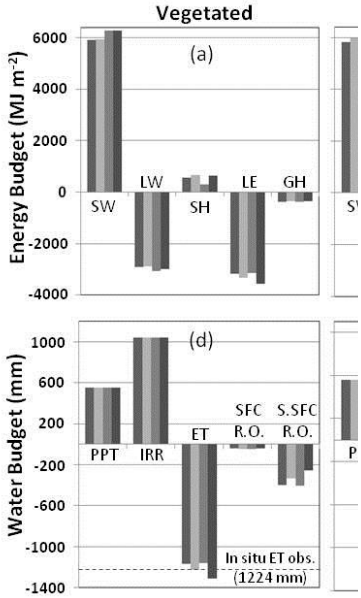

Table 1. Model scenarios (1-9) and the incorporated remotely sensed parameter sets.

	GVF	ISA	Albedo	LAI	Emissivity
Scenario 1 (Def. Par.)	-	-	-	-	-
Scenario 2 (R.S. GVF)	X	-	-	-	-
Scenario 3 (R.S. ISA)	-	X	-	-	-
Scenario 4 (R.S. Albedo)	-	-	X	-	-
Scenario 5 (R.S. LAI)	-	-	-	X	-
Scenario 6 (R.S. Emissivity)	-	-	-	-	X
Scenario 7 (R.S. Par. Group 1)	X	X	-	-	-
Scenario 8 (R.S. Par. Group 2)	-	-	X	X	X
Scenario 9 (R.S. Par. All)	X	X	X	X	X

Formatted Table